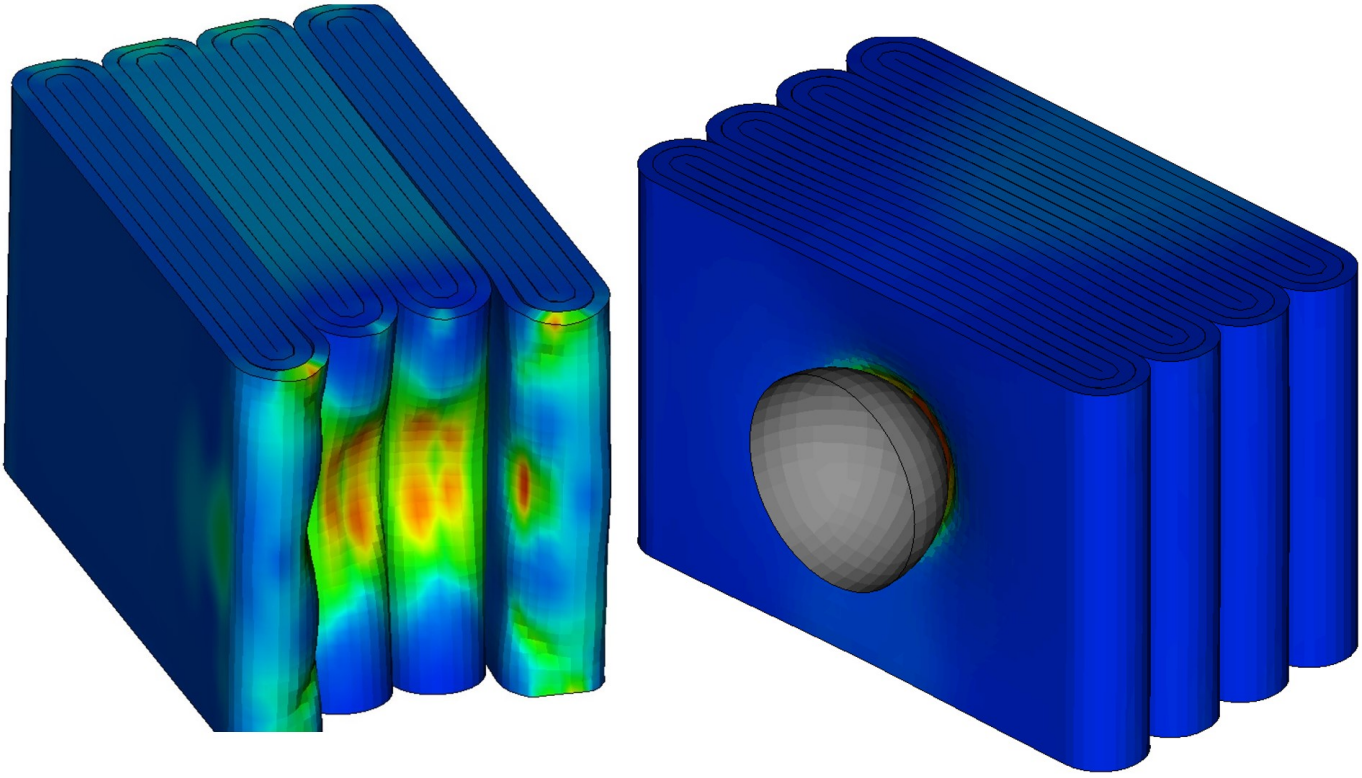

# Predicting short circuit of Li-ion battery cells during mechanical abuse

Master's Thesis in Applied Mechanics

Ankeet Mohan Purantagi

DEPARTMENT OF INDUSTRIAL AND MATERIALS SCIENCE

CHALMERS UNIVERSITY OF TECHNOLOGY
Gothenburg, Sweden 2024
www.chalmers.se

Master's thesis 2024

# Predicting short circuit of Li-ion battery cells during mechanical abuse

ANKEET MOHAN PURANTAGI


CHALMERS
UNIVERSITY OF TECHNOLOGY

Department of Industrial and Materials Science
*Division of Material and Computational Mechanics*
Chalmers University of Technology
Gothenburg, Sweden 2024

Predicting short circuit of Li-ion battery cells during mechanical abuse
ANKEET MOHAN PURANTAGI



Supervisor: Simon Vikström, David Carlstedt, Peter Gustavsson, Volvo Cars Corporation
Examiner: Fredrik Larsson, Industrial and Materials Science

Master's Thesis 2024
Department of Industrial and Materials Science
Division of Material and Computational Mechanics
Chalmers University of Technology
SE-412 96 Gothenburg
Telephone +46 31 772 1000

Cover: Battery cell material impact visualisation from LS-DYNA.

Typeset in LaTeX
Printed by Chalmers Reproservice
Gothenburg, Sweden 2024

# Preface

The report presented herein constitutes the culmination of my Master's thesis conducted at Volvo Cars Corporation as an integral component of the Applied Mechanics Master's programme. This thesis serves as a mandatory 30-credit course and was undertaken during the concluding semester of the two-year master's programme, spanning from January to June 2024.
The thesis was supervised by Prof. Fredrik Larsson and employees from Volvo Cars Simon Vikström, David Carlstedt, and Peter Gustavsson.

Predicting short circuit of Li-ion battery cells during mechanical abuse
Ankeet Mohan Purantagi
Department of Industrial and Materials Science
Chalmers University of Technology

# Abstract

Lithium-ion (Li-ion) batteries are today's preferred energy storage solution for electric vehicles (EVs). Ensuring safety in their design is crucial, especially in car accidents, where mechanical damage to battery cells can cause internal electric short circuits, posing significant risks. Thus, minimising the occurrence of such incidents is paramount. The growing adoption of EVs also heightens the risk of thermal runaway following crashes, whether from side, frontal, rear, or bottom impacts. This concern underscores the necessity of developing virtual testing models to mitigate the costs of real-life battery crash testing.

This thesis aimed to develop a finite element (FE) modelling methodology to predict internal short circuits in Li-ion batteries. The test data used in this work was obtained from previous tests, serving as the reference material behaviour response curve (force vs. displacement) upon which the subsequent research was based.

The study was conducted in two different loading directions. Four test cases (two for each loading direction) were considered to create a homogenised material model. Multiple parametric optimisation runs were performed better to fit the material model's response to the test. The final optimisation run achieved a realistic material behaviour that closely matched the test data. This single homogenised material model was then used to predict the short-circuit behaviour of the Li-ion battery in the specified scenarios.

The conclusions drawn from this thesis validate the assumption that the material behaves anisotropically, with the global response closely matching the test data. While the failure models used in these cases may apply to certain scenarios, there is a need for more test data to understand the material behaviour and its response better. This additional data will aid in developing the failure surface of the battery material. Given the complexity of battery material behaviour, future work should consider various other factors, such as internal pressure build-up, swelling effects, state of charge (SoC) and internal loads like buckling by increasing the number of resolved layers. These factors significantly influence the material response and should be explored further.

*Keywords*: Finite element modelling, Lithium-ion battery, failure models, crash simulations, material behaviour, electric vehicle, Anisotropic material, Short-circuit prediction, parametric optimisation.

# Acknowledgements

I would like to express my heartfelt appreciation and gratitude to my supervisors at Volvo Cars: Simon Vikström, David Carlstedt, and Peter Gustavsson. Their invaluable support and guidance throughout my thesis work have been instrumental in honing my skills and expanding my knowledge of battery technology, FEM, and crash simulations. I am deeply grateful for their experience and insights. Additionally, I would like to thank my engineering manager at Volvo Cars, Marie-Louise Holmer, for allowing me to undertake this thesis.

I am deeply grateful to my colleagues at Volvo Cars, Pulkit Sharma and Miroslav Svrcek, for their invaluable assistance in understanding material modelling and parameterization. I would also like to extend my sincere thanks to Priyatham Kareti, Mumtaz Alakkal, Kim Olander, Anton Stenstrand, Daniel Andersson, and Albin Knutsson for their support and help in mastering the FEM tools utilised during my thesis work.

I am deeply grateful to my examiner, Professor Fredrik Larsson, for his invaluable expertise and support throughout this thesis work. His feedback, insights, patience, and kindness have been profoundly motivating and helpful. Additionally, I would like to thank Professor Leif Asp for his valuable input and support during the monthly meetings and presentations.

Throughout my thesis work, my parents have been my steadfast pillars of support, offering unwavering encouragement and positivity over these six months. I am profoundly grateful to them. I would also like to extend my heartfelt thanks to my close friends and family for their support and understanding during the intense moments of this journey. Additionally, I am deeply thankful to BK Shivani Didi, whose virtual guidance has helped me overcome numerous challenges.

Thank you all for your support, care, and understanding.

Ankeet Mohan Purantagi, Gothenburg, June 2024

# List of Acronyms

Below is the list of acronyms that have been used throughout this thesis listed in alphabetical order:

| | |
|---|---|
| Li-ion | Lithium-ion |
| LiB | Lithium-ion battery |
| EVs | Electric vehicles |
| MPa | Megapascal(s) |
| LFP | Lithium Iron Phosphate |
| NMC | Nickle Manganese Cobalt Oxide |
| ISC | Internal short-circuit |
| FE | Finite element |
| SFA | Scale factor abscissa |
| SFO | Scale factor ordinate |
| RO | Mass density |
| LCID | Load curve ID |
| SOC | State of charge |
| ELFORM | Element formulation |

# Contents

# 1 Introduction

## 1.1 Background

Lithium-ion (Li-ion) batteries have emerged as the preferred option for storing energy in electric vehicles (EVs) owing to their advantageous electrochemical characteristics, e.g., a low self-discharge rate, high operating voltage, and high energy density compared to the other commercially available battery chemistries. Safety has always been of utmost importance in EV design, particularly in car accidents, where physical harm to battery cells can lead to electrical short circuits, posing potential safety hazards [1]. Hence, minimising the probability of such incidents in the EV design is crucial.

Frequently, vehicles are involved in accidents, and when it comes to EV collisions, the force exerted can lead to significant damage and displacement within the battery pack. The overall design and arrangement of the pack in an EV plays a crucial role in how the battery pack responds to a crash. This crash can cause substantial damage to sensitive internal components such as the separator due to the physical stress and strain experienced which can lead to short-circuits of the cell. Considering the inherently high energy density of Li-ion battery cells, such failures could result in unfavourable and severe consequences due to their low thermal stability, potentially triggering thermal runaway. Figure 1.1 illustrates the scenarios that can lead to the aforementioned thermal runaway.

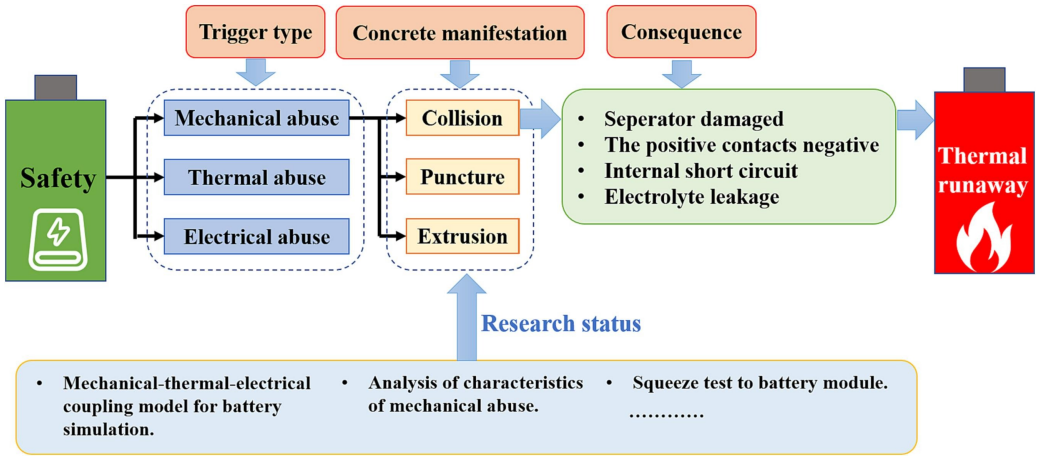


**Figure 1.1:** Possible scenarios leading to thermal runaway based on literature review. Reprint from: [2].

Thermal runaway is a phenomenon, where the heat generated by one exothermic reaction can trigger further reactions, leading to a self-sustaining increase in temperature. In extreme cases, this can ultimately lead to battery failure, leakage, or even combustion. An internal short circuit (ISC) happens when electrons can move quickly between the cathode and anode inside a battery cell due to direct contact between the electrodes. A plausible cause for an ISC is when there is a failure in the battery's internal components due to extensive deformation[3]. This occurrence is influenced by various factors, both internal, like lithium dendrite structure puncturing the separator [4], and external, such as mechanical, electrical, and thermal loads [3].

Extensive deformation and displacement as a result of applied force are referred to as external mechanical abuse situations, and vehicle crashes are one example in the case of electric vehicle applications. A basic schematic depicting the process by which Li-ion batteries fail when subjected to mechanical damage from the outside is shown in Figure 1.2. The scope of the thesis is limited to investigating ISC initiation due to separator failures. The separator failure mechanism is caused by over-stress in the separator, leading to a rupture in the separator material and thus causing a short circuit. The observed effects are high heat generation due to exothermic reactions, bloating of cell casing, and drastic voltage reduction [3].

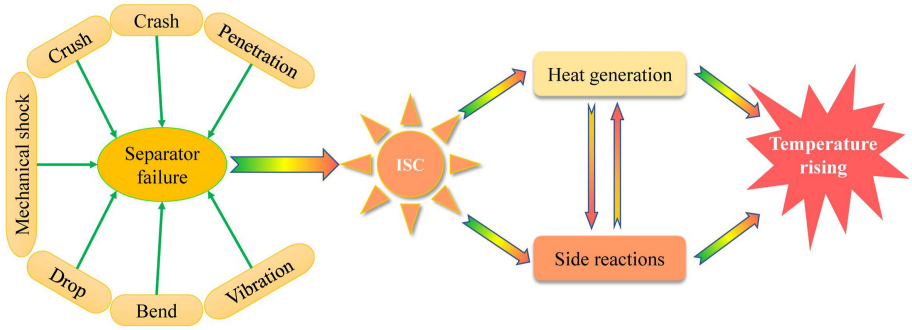


**Figure 1.2:** Schematic presentation of failure process of Li-ion batteries due to mechanical abuse. Reprint from:[5].

## 1.2 Objective

This thesis aims to develop a Finite Element (FE) modelling methodology to predict short circuits caused by mechanical abuse of Li-ion battery cells. The emphasis lies in developing an FE modelling strategy to analyse battery cells and modules, integrating established failure models.

## 1.3 Scope and limitations

Herein, the scope and limitations of this thesis are emphasised.

- ISC due to mechanical impact loading are studied.
- The test is conducted on Nickel Manganese Cobalt (NMC) based prismatic EV cells.
- The scope is limited to 2 simple loading scenarios as illustrated in the Figure 1.3 viz., in-plane (long-side) and out-of-plane (short-side) loading.
- Effective properties of the homogenised battery jelly roll model are considered during the crash analysis of the battery cell.
- Only quasi-static loading case is considered.
- The test was conducted on battery with a 100% state of charge (SOC).
- External test data from a parallel project is used to optimise the jelly roll material model.
- Variables such as state of health, manufacturing defects, temperature, and cell swelling over time are not evaluated.

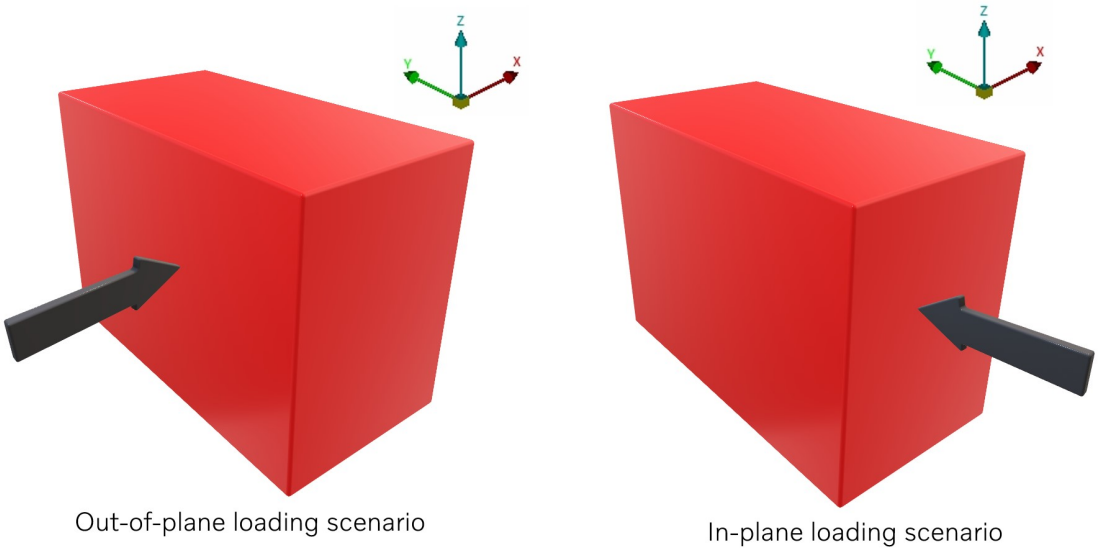


**Figure 1.3:** Loading scenarios studied during the thesis.

# 2

# Theory

## 2.1 Battery

A battery cell consists of one or more electrically connected electrochemical cells that store chemical energy in their two electrodes, the anode and the cathode. The battery converts the chemical energy into electrical energy on discharge. During discharge, electrons are released or absorbed at the electrodes, creating an electrical current that can be utilised externally.

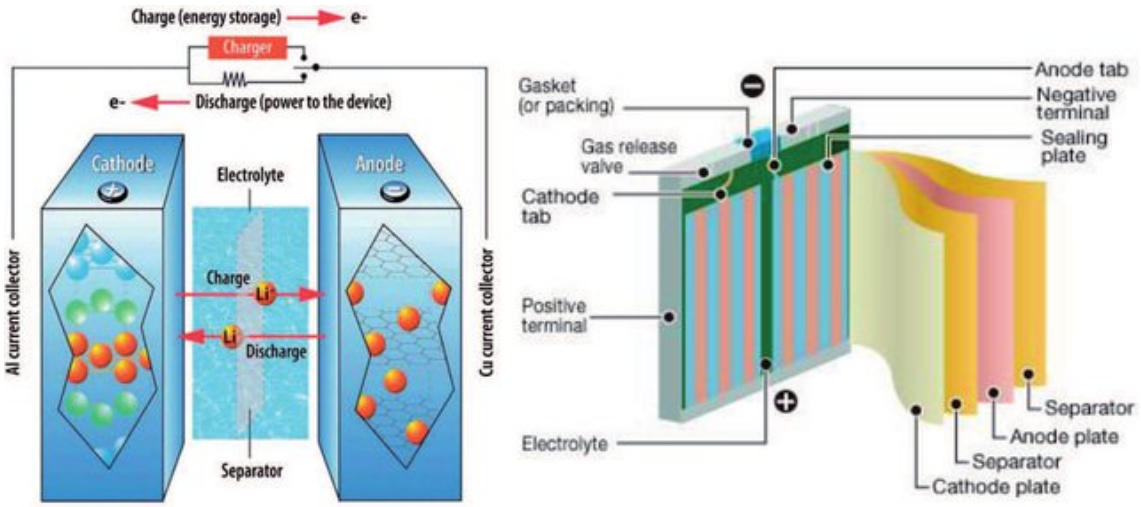


**Figure 2.1:** Structure of Li-ion battery. Reprint from: [6].

A typical Li-ion battery consists of 4 fundamental components viz., the anode (negative electrode), cathode (positive electrode), electrolyte, and separator as shown in Figure 2.1. Additional features such as current regulators, safety mechanisms, and temperature control systems may be incorporated depending on the specific battery type and intended application. Additionally, the battery casing provides structural support and protection against external factors. It is important to note that the arrangement and composition of these components can vary significantly based on the particular battery chemistry employed, such as lithium-ion, lead-acid, or nickel-metal hydride batteries.

## 2.2 Components of battery cells

### 2.2.1 Active materials

An active material refers to a substance that undergoes chemical reactions to convert chemical energy to electrical energy when the cell (dis)charges. The essential elements of a battery cell include the anode, and cathode materials, which collectively constitute its active components.

The anode, the negative electrode, consists of a copper foil used as the current collector, typically ranging in thickness from 8 to 18 $\mu$m. It is coated with a layer of negative electrode material, which acts as the active component. The active component here is typically graphite [7].
The cathode, the positive electrode, consists of an aluminium foil used as the current collector, typically ranging in thickness from 15 to 25 $\mu$m. It is coated with a positive electrode material layer, which acts as the active component. Examples of such materials include nickel-manganese-cobalt-oxide (NMC) or lithium-iron-phosphate (LFP) [7].

### 2.2.2 Electrolyte

The electrolyte is made up of salts, solvents, and additives and is a vital component in the functioning of a battery as it fills the interior of the cell. The salts act as conduits for lithium ions, the solvents are organic liquids that dissolve the salts and the additives enhance the performance. The electrolyte produced in this form only lets ions move between the electrodes and does not let electrons pass. After the assembly of the cell, the electrolyte is injected into it. Typically, the electrolyte comprises lithium hexafluorophosphate ($LiPF_6$) as the primary salt dissolved in a solvent like dimethyl carbonate (DMC). Additionally, various additives are blended in different proportions. The inclusion of these additives enhances the performance and safety characteristics of the electrolyte.

### 2.2.3 Current collectors

Current collectors serve dual purposes: providing structural support for electrode materials and facilitating electrical conduction between electrodes and the external circuit. In Li-ion batteries, various metals such as aluminium (Al), copper (Cu), nickel (Ni), titanium (Ti), and stainless steel act as current collectors. However, Al is predominantly employed for cathodes, while Cu is for anodes.

The primary reason aluminium is chosen for the positive electrode and copper for the negative electrode is due to the oxidation potential of these metals. Aluminium, used for the positive electrode, has a high oxidation potential, making it suitable for operating at high potentials. Conversely, copper, employed for the negative electrode, is easily oxidised under high potentials. Additionally, aluminium foil

develops a dense oxide film on its surface, which provides effective internal protection for the aluminium. Good conductivity and electrochemical stability are the other factors. The low density and advantageous mechanical characteristics of Al also help to improve the gravimetric energy density of batteries.

### 2.2.4 Separator

While the anode and cathode are the active materials and are responsible for the core functionality of a battery, a separator plays a critical role in guaranteeing the safety of a battery. A separator is an inactive fundamental component of a battery. For liquid electrolyte batteries, a separator is a multilayered, non-woven, micro-porous polymeric membrane placed between the anode and cathode to prevent their physical contact. The separator functions as a barrier, physically isolating the anode and cathode to prevent the direct flow of electrons and instead allows the flow of ions through the microscopic pores.

A separator should ideally have zero ionic resistance but infinite electronic resistance to separate the active materials effectively. However, in reality, separators have electrical resistivity ranging from $10^{12}$ to $10^{14}$ $\Omega$ cm [8], making them electrical insulators. Currently, the most widely employed separators are semi-crystalline polyolefin-based micro-porous separators.

## 2.3 Mechanical response of the battery cell

### 2.3.1 Anisotropic elasticity

Even while the linear elastic model can accurately represent many materials, some of them are not nearly isotropic. Examples include a variety of biological materials, wood, and composite materials. These materials respond differently mechanically in various directions. Anisotropic materials are those that exhibit this direction dependency.

A generalised form of Hooke's law relates stress to strain as $\{\sigma\} = [\boldsymbol{C}]\{\epsilon\}$, where $[\boldsymbol{C}]$ is a 6x6 matrix. Contracted notation streamlines express the stress-strain relationship in anisotropic materials:

$$\begin{Bmatrix} \sigma_1 \\ \sigma_2 \\ \sigma_3 \\ \sigma_4 \\ \sigma_5 \\ \sigma_6 \end{Bmatrix} = \begin{bmatrix} \boldsymbol{C}_{11} & \boldsymbol{C}_{12} & \boldsymbol{C}_{13} & \boldsymbol{C}_{14} & \boldsymbol{C}_{15} & \boldsymbol{C}_{16} \\ \boldsymbol{C}_{21} & \boldsymbol{C}_{22} & \boldsymbol{C}_{23} & \boldsymbol{C}_{24} & \boldsymbol{C}_{25} & \boldsymbol{C}_{26} \\ \boldsymbol{C}_{31} & \boldsymbol{C}_{32} & \boldsymbol{C}_{33} & \boldsymbol{C}_{34} & \boldsymbol{C}_{35} & \boldsymbol{C}_{36} \\ \boldsymbol{C}_{41} & \boldsymbol{C}_{42} & \boldsymbol{C}_{43} & \boldsymbol{C}_{44} & \boldsymbol{C}_{45} & \boldsymbol{C}_{46} \\ \boldsymbol{C}_{51} & \boldsymbol{C}_{52} & \boldsymbol{C}_{53} & \boldsymbol{C}_{54} & \boldsymbol{C}_{55} & \boldsymbol{C}_{56} \\ \boldsymbol{C}_{61} & \boldsymbol{C}_{62} & \boldsymbol{C}_{63} & \boldsymbol{C}_{64} & \boldsymbol{C}_{65} & \boldsymbol{C}_{66} \end{bmatrix} \begin{Bmatrix} \epsilon_1 \\ \epsilon_2 \\ \epsilon_3 \\ \epsilon_4 \\ \epsilon_5 \\ \epsilon_6 \end{Bmatrix} \tag{2.1}$$

where all strain components are (linearly) dependent upon each stress component. The notation is useful because it makes it possible to write the anisotropic elasticity equations in matrix form. The stress and strain are represented by a single subscript numbered between 1 and 6. The stiffnesses, or 36 $C'_{ij}s$, are material constants

that can ideally be discovered through experimentation. The stiffness matrix is the matrix of stiffnesses [9].
Because there are so many elastic constants in totally anisotropic materials, modelling them is challenging. Thankfully, there exist material symmetries in many non-isotropic materials that make the aforementioned calculations simpler. These categories of materials are explained next.

### 2.3.2 Orthotropic elasticity

An orthotropic material has three orthogonal planes of microstructural symmetry. The material symmetry inherent in the orthotropic material reduces the number of independent elastic constants to 9 [9] and the stiffness matrix is represented in eq. 2.2.

$$\begin{Bmatrix} \sigma_1 \\ \sigma_2 \\ \sigma_3 \\ \sigma_4 \\ \sigma_5 \\ \sigma_6 \end{Bmatrix} = \begin{bmatrix} \boldsymbol{C}_{11} & \boldsymbol{C}_{12} & \boldsymbol{C}_{13} & 0 & 0 & 0 \\ \boldsymbol{C}_{12} & \boldsymbol{C}_{22} & \boldsymbol{C}_{23} & 0 & 0 & 0 \\ \boldsymbol{C}_{13} & \boldsymbol{C}_{23} & \boldsymbol{C}_{33} & 0 & 0 & 0 \\ 0 & 0 & 0 & \boldsymbol{C}_{44} & 0 & 0 \\ 0 & 0 & 0 & 0 & \boldsymbol{C}_{55} & 0 \\ 0 & 0 & 0 & 0 & 0 & \boldsymbol{C}_{66} \end{bmatrix} \begin{Bmatrix} \epsilon_1 \\ \epsilon_2 \\ \epsilon_3 \\ \epsilon_4 \\ \epsilon_5 \\ \epsilon_6 \end{Bmatrix} \tag{2.2}$$

### 2.3.3 Elastoplasticity

In elastoplastic materials, at low-stress levels, the stress $\sigma_{ij}$ is only dependent on the state of stress; however, at higher stress states such as yield stress $\sigma_{yield}$ nonrecoverable plastic deformations are obtained. The yield stress changes with increasing plastic deformations, which are measured by internal variable $a_i$.

For a simplified uniaxial loading condition the Elasto-plasticity's main characteristics are explained below along with the stress-strain relation [10] as shown in Figure 2.2:

- When the stress is below the initial yield stress $\sigma_{\text{yield}}$, the material exhibits linear elastic behaviour, described by $\sigma = E\epsilon$. Consequently, the derivative of stress for strain is $\frac{d\sigma}{d\epsilon} = E$. During this phase, no plastic strain occurs, so the associated plastic flow rate is defined as $\dot{\epsilon}_p = 0$.
- If the stress $\sigma$ exceeds $\sigma_{\text{yield}}$ and continues to increase (loading), plastic (irreversible) strain $\epsilon_p$ and hardening will occur. The relationship between stress ($\dot{\sigma}$) and strain ($\dot{\epsilon}$) is given by including the hardening modulus $H$:

  $$\dot{\sigma} = \frac{EH}{E+H}\dot{\epsilon} \quad \text{and} \quad \frac{d\sigma}{d\epsilon} = \frac{EH}{E+H}. \tag{2.3}$$

  The development of plastic strain is expressed as:

  $$\dot{\epsilon}_p = \frac{\dot{\sigma}}{H}, \tag{2.4}$$

  and the yield stress increases (hardens) according to:

  $$\dot{\sigma}_{\text{yield}} = \dot{\sigma}. \tag{2.5}$$

- If the stress decreases (unloading), it follows:

$$\dot{\sigma} = E\dot{\epsilon}, \tag{2.6}$$

  with no development of plastic strain, hence $\dot{\epsilon}^p = 0$.
- When the material is fully unloaded ($\sigma = 0$), the remaining (residual) strain is represented by $\epsilon^p$.

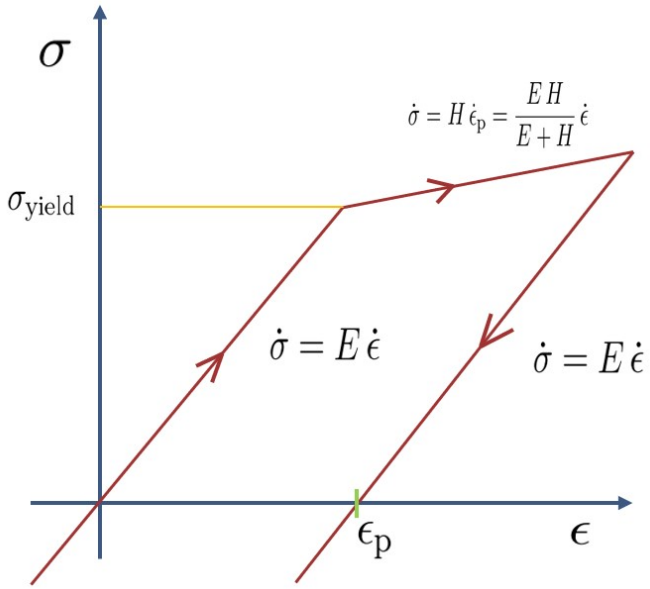


**Figure 2.2:** Stress v/s strain diagram for elastoplastic deformation of a continuum body.

To attain this kind of behaviour, the strains are decomposed into an elastic part and a plastic part

$$\epsilon = \epsilon_e + \epsilon_p \tag{2.7}$$

The stress $\sigma$ and elastic strain $\epsilon_e$ are assumed to have linear elastic relation.

$$\sigma = E\epsilon_e \ = E(\epsilon - \epsilon_p) \tag{2.8}$$

Then the yield function is formulated as isotropic hardening

$$\phi = |\sigma| - (\sigma_{yield} + \kappa) \tag{2.9}$$

where $\kappa$ is the hardening of yield stress. To indicate whether the material is undergoing loading or unloading, the following conditions are applied:

$$\Phi \text{ (yield function)} \leq 0, \quad \dot{\lambda} \text{ (plastic Lagrangian multiplier)} \geq 0, \quad \dot{\lambda}\Phi = 0 \tag{2.10}$$

The evolution of both plastic strain and hardening is formulated as

$$\dot{\epsilon}_p = \dot{\lambda}\frac{\sigma}{|\sigma|}, \text{ and } \dot{\kappa} = \dot{\lambda}H \tag{2.11}$$

### 2.3.4 Material Model

#### 2.3.4.1 Material Model - Modified Honeycomb

As the recommended element is 0 for the said material model, the LS-DYNA manual explains that for the said element formulation, the components of the stress tensor remain uncoupled and that the uncompressed elastic moduli are used [11]. For uncompacted material, the trial stress components are updated using the elastic interpolated moduli according to:

$$\sigma_{ii}^{n+1^{\text{trial}}} = \sigma_{ii}^{n} + E_{ii}\Delta\epsilon_{ii}, \qquad \sigma_{ij}^{n+1^{\text{trial}}} = \sigma_{ij}^{n} + 2G_{ij}\Delta\epsilon_{ij}, \tag{2.12}$$

$$\sigma_{jj}^{n+1^{\text{trial}}} = \sigma_{jj}^{n} + E_{jj}\Delta\epsilon_{jj}, \qquad \sigma_{jk}^{n+1^{\text{trial}}} = \sigma_{jk}^{n} + 2G_{jk}\Delta\epsilon_{jk}, \tag{2.13}$$

$$\sigma_{kk}^{n+1^{\text{trial}}} = \sigma_{kk}^{n} + E_{kk}\Delta\epsilon_{kk}, \qquad \sigma_{ki}^{n+1^{\text{trial}}} = \sigma_{ki}^{n} + 2G_{ki}\Delta\epsilon_{ki}. \tag{2.14}$$

The next step involves checking if the value has exceeded the permissible values determined from the load curves or not,

$$|\sigma_{ij}^{n+1^{\text{trial}}}| > \lambda\sigma_{ij}(\epsilon_{ij}) \tag{2.15}$$

$$\sigma_{ij}^{n+1} = \sigma_{ij}(\epsilon_{ij})\frac{\lambda\sigma_{ij}^{n+1^{\text{trial}}}}{|\sigma_{ij}^{n+1^{\text{trial}}}|} \tag{2.16}$$

$\sigma_{ij}$ is defined in the load curve for $xx$, $yy$, $zz$ stress components and $xy$, $yz$, $zx$ shear components. Strain rate in this context, refers to the Euclidean norm of the deviatoric strain rate tensor.
To address the issues identified with the original implementation of the transversely isotropic yield surface, the modified model allows for an independent adjustment of shear and hydrostatic resistance, without impacting the uniaxial compressive behaviour. Below is an explanation of the changes and how they can be incorporated into the model.
**Original Model Recap**: The uniaxial limit stress, $\sigma_y(\varphi, \epsilon_{\text{vol}})$, is given by:

$$\sigma_y(\varphi, \epsilon_{\text{vol}}) = \sigma_b(\varphi) + (\cos\varphi)^2\sigma_s(\epsilon_{\text{vol}}) + (\sin\varphi)^2\sigma_w(\epsilon_{\text{vol}})$$

Where:

- $\sigma_b(\varphi)$: Baseline stress function dependent on angle $\varphi$.
- $\sigma_s(\epsilon_{\text{vol}})$: Stress function considering volumetric strain, representing stiffening effects in the strong axis.
- $\sigma_w(\epsilon_{\text{vol}})$: Stress function considering volumetric strain, representing stiffening effects in the weak axis.

**Off-Angle Explanation**: In this context, the off-angle $\varphi$ refers to the angle between the loading direction and the material's strong axis. When $\varphi = 0°$, the loading is along the strong axis, and as $\varphi$ increases towards 90°, the loading becomes increasingly perpendicular to the strong axis.
**Modified Model Introduction**: To address the shear resistance issue, the new model introduces two additional terms: $\sigma_{\text{shear}}$ and $\sigma_{\text{hydro}}$, which allow for the independent tuning of shear and hydrostatic resistance.

**Modified Yield Surface Definition**: The modified uniaxial limit stress is now given by:

$$\sigma_y(\varphi, \epsilon_{\text{vol}}, \sigma_{\text{shear}}, \sigma_{\text{hydro}}) = \sigma_b(\varphi) + (\cos\varphi)^2\sigma_s(\epsilon_{\text{vol}}) + (\sin\varphi)^2\sigma_w(\epsilon_{\text{vol}}) + \sigma_{\text{shear}} + \sigma_{\text{hydro}}$$

**New Parameters**:

- $\sigma_{\text{shear}}$: An additional term representing shear resistance.
- $\sigma_{\text{hydro}}$: An additional term representing hydrostatic resistance.

**Implementation Details**:

- **Input Data**: The additional load curves for $\sigma_{\text{shear}}$ and $\sigma_{\text{hydro}}$ are given here. These curves describe how the shear and hydrostatic resistance vary with the volumetric strain which is described in the section 3.2.4.1.

**New Formulations and Recommendations**: The modified model (i.e., modified honeycomb as compared with the standard honeycomb) introduces novel parameters: the initial hydrostatic and shear limit stress values denoted as $\sigma_{\text{hydro}}$ and $\sigma_{\text{shear}}$ respectively, provided as GCAU and $|ECCU|$. The negative value of $|ECCU|$ serves as an indicator for the third yield surface option whenever the parameter defined by yield stress as a function of the angle off the material axis (LCA) is less than 0. This formulation implies that: (i) for uniaxial stress, the stress limit is determined by $\sigma_y(\varphi, \epsilon_{\text{vol}})$, (ii) for hydrostatic pressure, the stress limit is determined by $\sigma_{\text{hydro}}(\epsilon_{\text{vol}})$, and (iii) for simple shear, the stress limit is set by $\sigma_{\text{shear}}(\epsilon_{\text{vol}})$.

**Benefits**:

- **Increased Shear Resistance**: The addition of $\sigma_{\text{shear}}$ allows for increased shear resistance without altering the behaviour under uniaxial compression.
- **Enhanced Hydrostatic Control**: The $\sigma_{\text{hydro}}$ term allows for fine-tuning of the hydrostatic response, which can be crucial for materials that exhibit significant volumetric changes under load.

In summary, the modified model introduces additional parameters to control shear and hydrostatic resistance independently, thereby enhancing the material's performance in applications where shear collapse was previously an issue. This modification maintains the integrity of the uniaxial compressive behaviour while providing greater flexibility in material design and application.

## 2.4 Contact Mechanics

The considered loading on the battery is quasi-static and there is contact between a rigid body and a prismatic battery cell, the same contact is established between the internal components of the battery cell. So, it is important to understand the contact between the 2 solid bodies. Referring to the study material by Magnus Ekh et al., [12] classical mechanics provides analytical models for specific cases, with the Hertzian model being famous for contact between surfaces. However, advanced engineering demands more versatile approaches that can be integrated with computational methods.

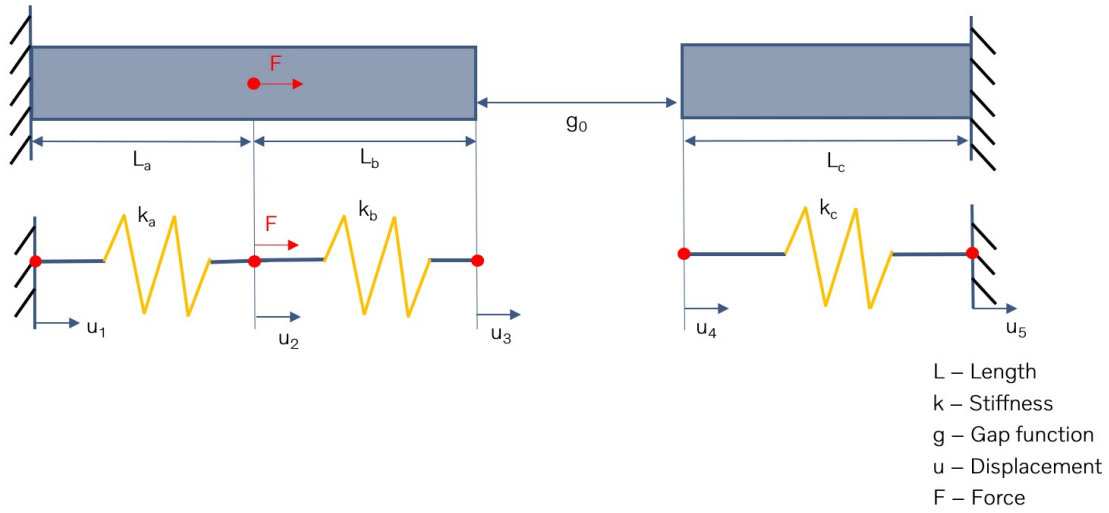


**Figure 2.3:** 2 bars contact problem.

Considering 2 bars in Figure 2.3 coming in contact where one bar is loaded with force F and the initial gap between the bars is $g_0$. We now discretise the bar as 3 different linear spring elements with a stiffness of $k_a = \frac{EA}{l_a}$, $k_b = \frac{EA}{l_b}$, and $k_c = \frac{EA}{l_c}$. The potential energy of the system can be expressed as

$$\Pi = \frac{1}{2}\left[k_a(u_2 - u_1)^2 + k_b(u_3 - u_2)^2 + k_c(u_5 - u_4)^2\right] |\mathrm{W}_{\mathrm{int}} - \mathrm{F}u_2|\mathrm{W}_{\mathrm{ext}} \tag{2.17}$$

with the essential boundary conditions $u_1 = u_5 = 0$ and the constraint condition $g = g_0 + u_4 - u_3 \geq 0$.
In case the bars are not in contact, variation of eq. (2.17) results in

$$\frac{\partial \Pi}{\partial u_2}\delta u_2 + \frac{\partial \Pi}{\partial u_3}\delta u_3 + \frac{\partial \Pi}{\partial u_4}\delta u_4 = 0, \quad \delta u_i \in U_0, \quad i = 2, 3, 4. \tag{2.18}$$

For the sake of brevity, we introduce the vector of free nodal displacements $\underline{\mathbf{u}}_F = [u_2, u_3, u_4]^T$ such that

$$\left(\frac{\partial \Pi}{\partial \underline{\mathbf{u}}_F}\right)^T \delta \underline{\mathbf{u}}_F = \delta \underline{\mathbf{u}}_F \frac{\partial \Pi}{\partial \underline{\mathbf{u}}_F} = \delta \underline{\mathbf{u}}_F^T \left(\underline{\mathbf{f}}_{\mathrm{int},F} - \underline{\mathbf{f}}_{\mathrm{ext},F}\right) = 0. \tag{2.19}$$

From eq 2.19, we can now construct the unconstrained system of equations

$$\begin{bmatrix} k_a & -k_a & 0 & 0 & 0 \\ -k_a & k_a + k_b & -k_b & 0 & 0 \\ 0 & -k_b & k_b + k_c & -k_c & 0 \\ 0 & 0 & -k_c & k_c & 0 \\ 0 & 0 & 0 & -k_c & k_c \end{bmatrix} \begin{bmatrix} u_1 \\ u_2 \\ u_3 \\ u_4 \\ u_5 \end{bmatrix} = \begin{bmatrix} F_1 \\ F \\ 0 \\ 0 \\ F_5 \end{bmatrix} \tag{2.20}$$

Here, $F_1$ and $F_5$ are unknown support forces. Consideration of the essential boundary conditions $u_1 = u_5 = 0$ allows us to condense the equation system such that

$$\begin{bmatrix} k_a + k_b & -k_b & 0 \\ -k_b & k_b + k_c & -k_c \\ 0 & -k_c & k_c \end{bmatrix} \begin{bmatrix} u_2 \\ u_3 \\ u_4 \end{bmatrix} = \begin{bmatrix} F \\ 0 \\ 0 \end{bmatrix} \tag{2.21}$$

or, more compactly,

$$\underline{\mathbf{K}}_{FF}\underline{\mathbf{u}}_F = \underline{\mathbf{f}}_F \tag{2.22}$$

The procedure to solve this contact problem is as follows:

1. Compute $\underline{\mathbf{u}}_F$ from eq. 2.21.
2. Check the contact condition $g := g_0 + u_4 - u_3 \geq 0$.
3. If $g \geq 0 \rightarrow$ no contact: $\underline{\mathbf{u}}_F$ is the solution, else $\rightarrow$ contact: modify the equation system using the Lagrange multiplier method or the penalty method.

### 2.4.1 Friction in contact

In the LS-DYNA tool, the frictional force calculation adheres to the method described by [13], which is based on Coulomb's law. Initially, $\mathbf{f}^*$ represents the trial force, $\mathbf{f}_n$ is the normal force, $k$ denotes the interference stiffness, $\mu$ is the coefficient of friction, and $\mathbf{f}^n$ is the frictional force at time $n$. To comprehend the friction calculation process in LS-DYNA, the following algorithm is explained according to the LS-DYNA manual [13]:

1. Determine the yield force, $F_y$:

$$F_y = \mu|\mathbf{f}_n| \tag{2.23}$$

2. Compute the incremental displacement of the slave node:

$$\Delta\mathbf{e} = \mathbf{r}_{n+1}(\xi_c^{n+1}, \eta_c^{n+1}) - \mathbf{r}_{n+1}(\xi_c^n, \eta_c^n) \tag{2.24}$$

where $\xi_c$ and $\eta_c$ are the contact point coordinates.

3. Update the interface force to a trial value:

$$\mathbf{f}^* = \mathbf{f}_n - k\Delta\mathbf{e} \tag{2.25}$$

4. Verify the yield condition:

$$\mathbf{f}_{n+1} = \mathbf{f}^* \quad \text{if} \quad |\mathbf{f}^*| \leq F_y \tag{2.26}$$

5. Adjust the trial force if it exceeds the yield force:

$$\mathbf{f}_{n+1} = \frac{F_y}{|\mathbf{f}^*|}\mathbf{f}^* \quad \text{if} \quad |\mathbf{f}^*| > F_y \tag{2.27}$$

To smooth the transition between the static friction coefficient, $\mu_s$, and the dynamic friction coefficient, $\mu_d$, an exponential interpolation function is used, where $\mathbf{v}$ is the relative velocity between the slave node and the master segment:

$$\mu = \mu_d + (\mu_s - \mu_d)e^{-c|\mathbf{v}|} \tag{2.28}$$

where

$$\mathbf{v} = \frac{\Delta\mathbf{e}}{\Delta t} \tag{2.29}$$

Here, $\Delta t$ is the time step size, and $c$ is a decay constant. The interface shear stress due to Coulomb friction can become very high, potentially exceeding the material's capacity. Therefore, an additional limit on the tangential force is applied:

$$\mathbf{f}_{n+1} = \min(\mathbf{f}_{n+1}^{\text{Coulomb}}, \kappa A_{\text{master}}) \tag{2.30}$$

where $A_{\text{master}}$ is the area of the master segment and $\kappa$ is the viscous coefficient. It is acknowledged that multiple nodes might contribute to the shear stress of a segment, and the stress may still exceed the limit $\kappa$.

### 2.4.2 Penalty Method

The LS-Dyna tool uses the penalty method to solve the contact mechanics problem, this section provides the theory behind the said penalty method. To penalise contact, we expand such that

$$\Pi = W_{\text{int}} + \frac{1}{2}\varepsilon g^2 - W_{\text{ext}}.(10.23) \tag{2.31}$$

Hence, for example in Figure 2.3 we insert an elastic spring into the system to penalise penetration of node 3 with node 4. As outlined above, this corresponds to the stiffness of that spring. Note that, in the case of penetration, the gap function $g = g_0 + u_4 - u_3 < 0$. Now, the equation system reads

$$\begin{bmatrix} k_a + k_b & -k_b & 0 \\ -k_b & k_b + \epsilon & -\epsilon \\ 0 & -\epsilon & k_c + \epsilon \end{bmatrix} \begin{bmatrix} u_2 \\ u_3 \\ u_4 \end{bmatrix} = \begin{bmatrix} F \\ \varepsilon g_0 \\ -\varepsilon g_0 \end{bmatrix} \tag{2.32}$$

In LS-DYNA, contact is represented by a linear spring between the slave nodes and the nearest master segments. The stiffness of these springs dictates the force applied to both the slave and master nodes. The method for calculating the contact spring stiffness for solid elements is shown in eq. 2.33, and for shell elements in Equation 2.34. [11]

$$k = \frac{fs \cdot Area^2 \cdot K}{Volume} \tag{2.33}$$

$$k = \frac{fs \cdot Area \cdot K}{MaximumDiagonal} \tag{2.34}$$

$Area$ is the area of contact segment

$K$ is the bulk modulus contacted element

$fs$ is the $SLSFAC$ **x** $SFS$

$SLFAC$ is the penalty scale factor $(0.1\ by\ default)$

$SFS$ is the scale factor on default slave stiffness

#### 2.4.2.1 Strong form for contacts

$$-\boldsymbol{\sigma} \cdot \nabla = \mathbf{b} \quad \text{in } \Omega \tag{2.35}$$

$$\mathbf{u} = \mathbf{u}_D \quad \text{on } \Gamma_D \tag{2.36}$$

$$\mathbf{t} := \boldsymbol{\sigma} \cdot \mathbf{n} = \mathbf{t}_N \quad \text{on } \Gamma_N \tag{2.37}$$

$$\mathbf{t} := \boldsymbol{\sigma} \cdot \mathbf{n} = p_N \cdot \mathbf{N} \quad \text{on } \Gamma_C \tag{2.38}$$

$$g(u) \geq 0 \quad \text{on } \Gamma_C \tag{2.39}$$

$$p_n \geq 0 \quad \text{on } \Gamma_C \tag{2.40}$$

$$gp_n = 0 \quad \text{on } \Gamma_C \tag{2.41}$$

In this context, we assume a small strain elasticity model where the stress tensor $\boldsymbol{\sigma}$ is a function of the strain tensor $\boldsymbol{\epsilon}[\boldsymbol{u}]$, ($\boldsymbol{\sigma} = \boldsymbol{\sigma}(\boldsymbol{\epsilon}[\boldsymbol{u}])$; $\boldsymbol{\epsilon}[\boldsymbol{u}] := [\boldsymbol{u} \otimes \boldsymbol{\nabla}]^{\text{sym}}$). Following conventional notation, $\mathbf{b}$ represents the body force, while $\mathbf{t_p}$ and $\mathbf{u_p}$ correspond to Neumann and Dirichlet boundary conditions, respectively. For the portion of the boundary that may be in contact, denoted by $\Gamma_C$, $g(u)$ represents the gap function, and $N$ signifies the contact normal.

$$\mathbf{N} := \frac{\partial g}{\partial u} \tag{2.42}$$

Finally, $p_n$ defines the contact pressure.

#### 2.4.2.2 Weak form for contacts

The weak format of the static equilibrium is written as

$$\int_\Omega \sigma : \epsilon[u]\, \delta u \, \mathrm{d}\Omega - \int_\Omega b \cdot \delta u \, \mathrm{d}\Omega - \int_{\Gamma_t} t \cdot \delta u \, \mathrm{d}\Gamma - \int_{\Gamma_C} p_N \cdot N \, \delta u \, \mathrm{d}\Gamma = 0 \tag{2.43}$$

As a first step, we establish the "unconstrained" potential

$$\Pi(u) = \int_\Omega \psi(\epsilon[u]) \, \mathrm{d}\Omega - \int_\Omega b \cdot u \, \mathrm{d}\Omega - \int_{\Gamma_t} t \cdot u \, \mathrm{d}\Gamma \tag{2.44}$$

where $\psi(\epsilon)$ is the strain energy density such that $\sigma = \partial\psi/\partial\epsilon$.

$$\Pi'(u; \delta u) - \int_{\Gamma_C} p_N \cdot N \, \delta u \, \mathrm{d}\Gamma = 0 \tag{2.45}$$

Secondly, we shall assume that we know where contact is active, thus we shall set

$$g(u) = 0 \quad \text{on } \hat{\Gamma}_C, \tag{2.46}$$

$$p_N = 0 \quad \text{on } \Gamma_C \backslash \hat{\Gamma}_C. \tag{2.47}$$

where $\hat{\Gamma}_C \subseteq \Gamma_C$ is the part in active contact. We introduce the penalty term to augment the potential as follows:

$$\Pi^\epsilon(u) = \Pi(u) + \int_{\hat{\Gamma}_C} \frac{\epsilon}{2} \left(g(u)\right)^2 \, \mathrm{d}\Gamma. \tag{2.48}$$

In this expression, $\epsilon (= \epsilon(x))$ is a penalty parameter. Minimizing the augmented potential leads to a solution that increasingly adheres to the constraint as $\epsilon \to \infty$. Consequently, we approximate

$$u^\epsilon = \arg\min_{\hat{u}} \Pi^\epsilon(\hat{u}), \tag{2.49}$$

where $u^\epsilon \to u$ (the solution obtained using the Lagrange multiplier method) as $\epsilon \to \infty$.
The corresponding variational form is obtained by finding $u \in \mathbf{U}$ such that

$$\int_\Omega \boldsymbol{\sigma} : \epsilon[\delta u]\,\mathrm{d}\Omega + \int_{\hat{\Gamma}_C} \epsilon g(u)\frac{\partial g}{\partial u}\cdot\delta u\,\mathrm{d}\Gamma = \int_\Omega \mathbf{b}\cdot\delta u\,\mathrm{d}\Omega + \int_{\Gamma_N} \mathbf{t}\cdot\delta u\,\mathrm{d}\Gamma \quad \forall \delta u \in \mathbf{U}^0. \tag{2.50}$$

Recognizing that $N = \frac{\partial g}{\partial u}$, we can identify the pressure as

$$p_N = \epsilon(-g(u)). \tag{2.51}$$

The displacement field and the corresponding test function are discretized as

$$\mathbf{u}_h = \sum_k N_k^{(\mathbf{u})}(x)(\mathbf{a})_k, \quad \delta\mathbf{u}_h = \sum_k N_k^{(\mathbf{u})}(x)(\delta\mathbf{a})_k, \tag{2.52}$$

where $N_k^{(\mathbf{u})}(x)$ are the finite element basis functions, $\mathbf{a}$ is the nodal displacement vector, and $\delta\mathbf{a}$ is the nodal vector of the test functions. For simplicity, we assume homogeneous Dirichlet boundary conditions ($u = 0$ or $\mathbf{U} = \mathbf{U}^0$).
Here the nodal collocation for the contact constraints, expressed as

$$\int_{\hat{\Gamma}_C} \epsilon g(u)\frac{\partial g}{\partial u}\cdot\delta u\,d\Gamma \approx \sum_{i=1}^{n_C} \epsilon_i s_i g_{s_i}(\mathbf{a}) \sum_k \left(\frac{\partial g_{s_i}}{\partial \mathbf{a}_k}(\delta\mathbf{a}_k)\right), \tag{2.53}$$

where $\epsilon_i$ denotes the discrete contact spring attached to node $s_i$.
Testing with arbitrary test displacements $\delta\mathbf{a}$, the discrete equation is

$$\mathbf{f}_{\text{int}}(\mathbf{a}) + \mathbf{f}_C(\mathbf{a}) = \mathbf{f}_{\text{ext}}, \tag{2.54}$$

where the added "penalty" force is

$$(\mathbf{f}_C)_k = \sum_{i=1}^{n_C} \epsilon_i s_i g_{s_i}(\mathbf{a})\frac{\partial g_{s_i}}{\partial \mathbf{a}_k}, \tag{2.55}$$

and the standard FE-vectors are given by

$$(\mathbf{f}_{\text{int}})_k = \int_\Omega \boldsymbol{\sigma} : \epsilon[N_k^{(\mathbf{u})}]\,d\Omega, \tag{2.56}$$

$$(\mathbf{f}_{\text{ext}})_k = \int_\Omega \mathbf{b}\cdot N_k^{(\mathbf{u})}\,d\Omega + \int_{\Gamma_N} \mathbf{t}\cdot N_k^{(\mathbf{u})}\,d\Gamma. \tag{2.57}$$

**Remark.** The penalty force can be reformulated as

$$\mathbf{f}_C = \mathbf{C}^{\mathbf{T}}\boldsymbol{\epsilon}\mathbf{C}\mathbf{g}_C, \tag{2.58}$$

where

$$(\boldsymbol{\epsilon})_{ij} = \begin{cases} \epsilon_i & \text{for } j = i \\ 0 & \text{for } j \neq i \end{cases},$$
$$(\mathbf{g}_C)_i = g_{s_i}(\mathbf{a}),$$
$$(\mathbf{C})_{ij,k} = \frac{\partial g_{s_i}}{\partial \mathbf{a}_k}.$$

## 2.5 Element Formulation

### 2.5.1 Reduced Intergration

To address locking in finite element analysis, one method involves augmenting the deformation gradient by making reasonable assumptions, resulting in an assumed strain element with a deformation gradient denoted as $\mathbf{F}_{as}$. This approach has certain constraints, the most significant being the need to ensure frame invariance. This can be achieved by ensuring that the assumed velocity gradient, $\mathbf{L}_{as} = \dot{\mathbf{F}}_{as}\mathbf{F}_{as}^{-1}$, remains skew-symmetric when elements undergo rigid body motion [13].
A simple example of this approach is to assume that the deformation gradient remains constant throughout an element, either as its value at the center ($\mathbf{F}_{as} = \mathbf{F}_0$) or as its integrated mean ($\mathbf{F}_{as} = \overline{\mathbf{F}}$). This assumption can alleviate locking but results in an incomplete element because non-rigid deformation modes do not generate strains; in other words, the symmetric part of $\mathbf{L}_{as}$ is zero. These elements require artificial stabilisation, known as hourglass control, and are implemented in LS-DYNA [13].
A more refined approach involves assuming that only the volumetric part of the deformation gradient is constant, while the deviatoric part remains unaffected. This method, known as selective reduced integration, is available as type 2 elements in LS-DYNA. The deformation gradient is expressed as $\mathbf{F}_{as} = (J_0/J)^{1/3}\mathbf{F}$ or $\mathbf{F}_{as} = (\overline{J}/J)^{1/3}\mathbf{F}$ depending on the averaging choice, where $J = \det(\mathbf{F})$ is the Jacobian. The choice of $\overline{J}$ is preferred because it ensures the element passes the patch test, unlike $J_0$ [13].
While this selective reduced integration element reduces volumetric locking, it can still exhibit high stiffness in shear, especially in elements with poor aspect ratios. A heuristic method to address this issue is presented by Borrvall (2009) [13].

#### 2.5.1.1 Hourglass control

One major limitation of one-point integration in finite element analysis is the challenge of managing zero energy modes, commonly referred to as hourglass modes. These undesirable modes typically have periods significantly shorter than the primary structural response periods and often manifest as oscillatory behaviours. However, hourglass modes with periods similar to the structural response periods can be stable components of the overall deformation modes and should be permitted. To mitigate undesirable hourglassing effects, methods such as viscous damping or introducing a small elastic stiffness can be employed. This strategy can effectively prevent the emergence of anomalous modes while minimally affecting the stable global modes.
The early three-dimensional techniques for controlling hourglass modes were pioneered by Kosloff and Frazier (1974) and Wilkins et al. (1974). Since hourglass deformation modes are orthogonal to strain calculations, the work done by the hourglass resistance is not accounted for in the energy equation, potentially leading to a slight loss of energy. Despite this, implementing hourglass control is always advisable for under-integrated solid elements to ensure the accuracy and stability of simulations[13].

It is simple to understand why hourglass modes form. Consider the strain rate calculations for an 8-node solid element given by:

$$\dot{\epsilon}_{ij} = \frac{1}{2}\left(\sum_{k=1}^{8} \frac{\partial \phi_k}{\partial x_i}\dot{x}_j^k + \frac{\partial \phi_k}{\partial x_j}\dot{x}_i^k\right). \tag{2.59}$$

When diagonally opposite nodes have identical velocities, such as:

$$\dot{x}_i^1 = \dot{x}_i^7, \quad \dot{x}_i^2 = \dot{x}_i^8, \quad \dot{x}_i^3 = \dot{x}_i^5, \quad \dot{x}_i^4 = \dot{x}_i^6, \tag{2.60}$$

the strain rates become zero:

$$\dot{\epsilon}_{ij} = 0, \tag{2.61}$$

due to the asymmetries in the shape function derivatives. This can be shown by proving the orthogonality of the hourglass shape vectors. The derivatives of the shape functions:

$$\sum_{k=1}^{8} \frac{\partial \phi_k}{\partial x_i}\Gamma_{\alpha k} = 0, \quad i = 1, 2, 3, \quad \alpha = 1, 2, 3, 4. \tag{2.62}$$

The product of the base vectors with the nodal velocities is zero when the element velocity field lacks an hourglass component:

$$h_{i\alpha} = \sum_{k=1}^{8} \dot{x}_i^k \Gamma_{\alpha k} = 0. \tag{2.63}$$

However, these products are nonzero if hourglass modes are present. The 12 hourglass-resisting force vectors, $f_{i\alpha k}$, are designed to counteract these modes.

The 12 hourglass-resisting force vectors, $\mathbf{f}_{i\alpha k}$, are given by:

$$f_{i\alpha}^k = a_h h_{i\alpha} \Gamma_{\alpha k}, \tag{2.64}$$

where

$$a_h = Q_{HG} \rho v_e^{2/3} \frac{c}{4}, \tag{2.65}$$

In this context, $v_e$ denotes the element volume, $c$ represents the material sound speed, and $Q_{HG}$ is a user-defined constant, typically set within the range of 0.05 to 0.15. Additionally, $\rho$ stands for the specific mass density. One limitation of hourglass control type 1 is that its resisting forces do not align with the linear velocity field unless the elements have a parallelepiped shape. Flanagan and Belytschko (1981) developed a method to counteract all modes except those with zero energy. Their approach involves resisting components of the velocity field that do not adhere to a fully linear pattern, referred to as the hourglass velocity field. This method effectively addresses the issue by targeting the non-linear components of the velocity field, ensuring more accurate and stable simulations.

$$\dot{x}_i^{k^{HG}} = \dot{x}_i^k - \dot{x}_i^{k^{LIN}}, \tag{2.66}$$

where

$$\dot{x}_i^{k^{LIN}} = \bar{\dot{x}}_i + \bar{\dot{x}}_{i,j}(x_j^k - \bar{x}_j), \tag{2.67}$$

$$\bar{x}_i = \frac{1}{8}\sum_{k=1}^{8} x_i^k, \quad \bar{\dot{x}}_i = \frac{1}{8}\sum_{k=1}^{8} \dot{x}_i^k. \tag{2.68}$$

Flanagan and Belytschko devised hourglass shape vectors specifically tailored to the geometry of the elements, ensuring they are orthogonal to both the fully linear velocity field and rigid body motion. These vectors are designed to counteract hourglass velocity deformations. The hourglass shape vectors are defined in terms of base vectors as follows:

$$\gamma_{\alpha k} = \Gamma_{\alpha k} - \phi_{k,i}\sum_{n=1}^{8} x_i^n \Gamma_{\alpha n}, \tag{2.69}$$

the analogue for Equation (2.63) is:

$$g_{i\alpha} = \sum_{k=1}^{8} \dot{x}_i^k \gamma_{\alpha k} = 0, \tag{2.70}$$

with the 12 resisting force vectors being:

$$f_{i\alpha k} = a_h g_{i\alpha} \gamma_{\alpha k}. \tag{2.71}$$

The various types of hourglass control methods in LS-DYNA [13] offer different approaches to mitigating hourglassing effects, which can arise during simulations involving solid elements.
Type 1 hourglass control, the default option, employs a viscosity-based approach, which involves additional computational costs. Although it may provide a faster solution for very regular meshes.
Type 2 and Type 3 hourglass controls are similar, with the main difference being the evaluation of shape function derivatives at the element's centroid rather than its origin. While Type 3 ensures exact element volume, it may require more computations due to the lack of anti-symmetry.
Types 4 and 5, like Types 2 and 3, respectively, evaluate hourglass stiffness instead of viscosity. Hourglass rates are multiplied by the solution time step to calculate hourglass deformation increments, with the stiffness scaled to maintain stability.
Type 6 hourglass control represents an advancement over Type 5 by matching hourglass forces with those of fully integrated elements. This is achieved through closed-form integration over the element volume and scaling the stiffness accordingly. Developed by Belytschko and Bindeman (1993), this method prevents element locking with nearly incompressible materials. It is recommended to adjust the user-defined hourglass constant $a_h$ based on material properties, with 1.0 providing accurate stiffness for elastic materials and a smaller value suggested for nonlinear materials.
In summary, the choice of hourglass control method depends on factors such as computational efficiency, accuracy requirements, and material properties, with Type 6 offering improved accuracy and versatility for both implicit and explicit solutions.

#### 2.5.1.2 Co-rotational coordinate system

In large displacement formulations, distinguishing between deformation and rigid body displacements is crucial for accurate strain and energy computations. This is achieved by comparing the current configuration of a deformed body with a reference configuration, which can be its initial or previous state. While total deformations are computed by comparing with the initial configuration, incremental deformations result from comparisons with the previous configuration, commonly preferred for their computational advantages [13].
Directly comparing configurations yields displacements comprising both deformation and rigid body motion components, necessitating their separation. Deformations are typically obtained by subtracting estimates of rigid body displacements, often approximated in co-rotational formulations. These formulations utilise element and body coordinate systems to track deformations accurately while updating local axes at each time step to account for changes in the unit vector triad with the element's deformation.

## 2.6 Galerkin approximation for explicit dynamic computation

The following strong-form equation describes the initial/boundary value problem for elastodynamics:

$$\rho \ddot{\boldsymbol{u}} = \nabla \cdot \boldsymbol{\sigma} + \boldsymbol{f}_b \quad \text{in } \Omega, \tag{2.72}$$

where $\rho$ is the mass density, $\ddot{\boldsymbol{u}}$ is the acceleration, $\nabla \cdot \boldsymbol{\sigma}$ is the divergence of the stress tensor $\boldsymbol{\sigma}$, and $\boldsymbol{f}_b$ is the body force vector.
The boundary conditions are:

$$\mathbf{u} = \mathbf{u}^p \quad \text{on } \Gamma_u, \tag{2.73}$$

$$\boldsymbol{\sigma} \cdot \mathbf{n} = \mathbf{h} \quad \text{on } \Gamma_h, \tag{2.74}$$

where $\mathbf{u}$ is the displacement, $\Gamma_u$ is the portion of the boundary where displacements are prescribed, $\Gamma_h$ is the portion of the boundary where tractions are prescribed, $\mathbf{n}$ is the unit normal vector on $\Gamma_h$, and $\mathbf{h}$ is the traction vector.
The initial conditions are:

$$\mathbf{u}(\mathbf{X}, 0) = \mathbf{u}^p(\mathbf{X}), \tag{2.75}$$

$$\dot{\mathbf{u}}(\mathbf{X}, 0) = \dot{\mathbf{u}}^p(\mathbf{X}), \tag{2.76}$$

where $\mathbf{u}_0(\mathbf{X})$ is the initial displacement field and $\dot{\mathbf{u}}_0(\mathbf{X})$ is the initial velocity field.

### 2.6.1 Weak formulation with assumed strain method

An assumed strain method is employed to incorporate the Lagrangian strain smoothing formulation into the Galerkin approximation. This transforms the problem into its weak form:

$$\int_\Omega \rho \delta \mathbf{u} \cdot \ddot{\mathbf{u}} \, d\Omega + \int_\Omega \delta \tilde{\boldsymbol{\epsilon}} : \boldsymbol{\sigma} \, d\Omega = \int_\Omega \delta \mathbf{u} \cdot \mathbf{f}_b \, d\Omega + \int_{\Gamma_h} \delta \mathbf{u} \cdot \mathbf{h} \, d\Gamma, \tag{2.77}$$

where $\delta\mathbf{u}$ is the virtual displacement, and $\delta\tilde{\boldsymbol{\epsilon}}$ is the virtual assumed strain.

### 2.6.2 Explicit Time Integration

For explicit time integration, the equations to be solved are:

$$\delta\mathbf{u}^T\mathbf{M}\ddot{\mathbf{u}} = \delta\mathbf{u}^T\mathbf{R}, \tag{2.78}$$

where

$$\ddot{\mathbf{u}}_I = [\ddot{d}_{1I}, \ddot{d}_{2I}, \ddot{d}_{3I}]^T \text{ represents the nodal accelerations,} \tag{2.79}$$

$$\mathbf{M}_{IJ} = \int_\Omega \rho\Psi_I(\mathbf{x})\Psi_J(\mathbf{x})\,d\Omega = \int_{\Omega_0} \rho_0\Psi_I(\mathbf{X})\Psi_J(\mathbf{X})\,d\Omega \text{ is the mass matrix,} \tag{2.80}$$

$$\mathbf{R}_I = \int_\Omega \mathbf{B}_I^T(\mathbf{x})\cdot\boldsymbol{\sigma}(\tilde{\mathbf{F}})\,d\Omega - [\Psi_I(\mathbf{x})\mathbf{h}]\Big|_{\Gamma_h} - \int_\Omega \Psi_I(\mathbf{x})\mathbf{f}_b\,d\Omega \text{ is the internal force vector.} \tag{2.81}$$

Here,

- $\mathbf{B}_I^T(\mathbf{x})$ is the smoothed gradient matrix derived from the assumed strain method.
- $\tilde{\mathbf{F}}$ represents the deformation gradient.
- $\mathbf{u}_I$ and $\dot{\mathbf{u}}_I$ are the nodal displacement and velocity vectors, respectively.

This formulation ensures the stability and accuracy of the finite element solution by incorporating the Lagrangian strain smoothing and assumed strain methods, addressing issues such as locking and hourglassing in numerical simulations [13].

## 2.7 Internal short-circuit mechanisms

Internal short circuits in a battery can result from various factors such as crushing, penetration, overcharging, over-discharging, overheating, dendrite formation, and separator misalignment. According to Zhang et al., [5], primary ISC triggering factors include internal defects, mechanical abuse, over-discharge, over-charge, and over-temperature. Despite varying pathways, these triggers can all lead to ISC. However, separator failure is an ongoing risk, posing a substantial threat to EVs. Figure 2.4 provides a basic illustration of various ISC trigger factors.

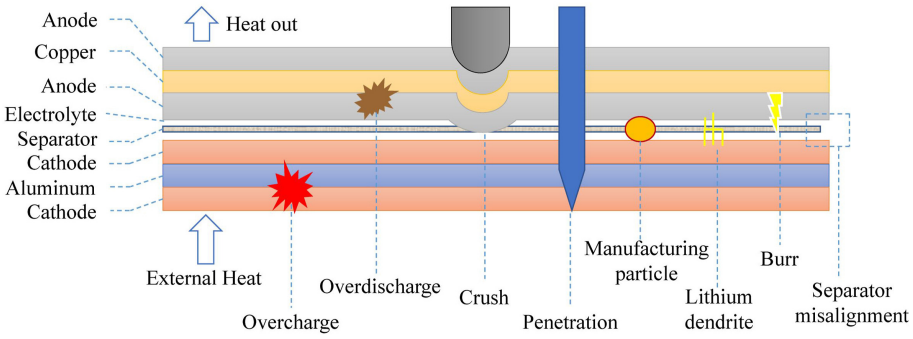


**Figure 2.4:** Example illustrating the ISC triggering factors in Li-ion Battery (LiB): Reprint from [5].

### 2.7.1 Failure mechanism due to mechanical abuse

Referring to Zhu et al. [14] the deformation and failure mechanism of Li-ion battery cells under indentation (out-of-plane) loading occurs in 5 different stages. The illustration shown in Figure 2.5 gives a schematic representation of a Li-ion cell's deformation and failure mechanism under mechanical abuse.

The stages of deformation and failure mechanisms explained in the paper [14] are discussed briefly below:
Stage I: During indentation testing, a uniform displacement field forms upon contact with the indenter, leading to immediate deformation of the cell surface. Continuous compression causes deformation to increase, resulting in various localizations such as strain and stress. Additionally, compression reduces interlayer spacing.

Stage II: Continuous compression further compacts bonded aggregates, reducing interlayer distance. Active materials are pushed out due to radial displacement, enhancing stretching in metal foils and inducing bending-type deformation. Shear bands form, influenced by indenter parameters and interlayer distance.

Stage III: Macro cracks in bonded aggregates reach metal foils, localizing tensile stresses and causing in-plane ductile fracture. Indentation leads to dilation, change in shear band angle, and extension in ductile fracture. Circumferential stress and radial displacement increase, leading to elongated radial cracks in copper foil and buckling across layers.

Stage IV: Increased load causes mud cracks in copper foil and extends macro cracks to the separator. Shear bands progress, causing irregular kinks and cusps at boundaries. The separator experiences continuous jamming and sharpening. More layers undergo buckling.

Stage V: Extensive internal ductile fracture and anti-plane shear-induced ductile fracture occur in aluminium foil. Contact between fault lines in opposite polarity electrodes forms a global fault line. Global strain localisation exacerbates separator failure, potentially leading to short circuits between electrodes.

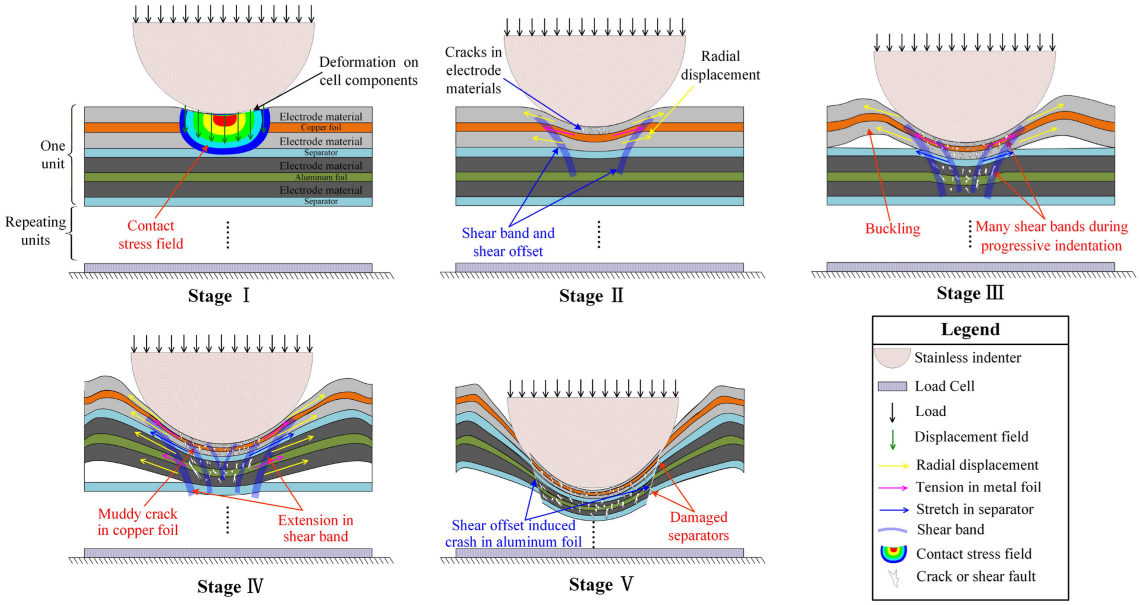


**Figure 2.5:** Schematic of the failure mechanism in a LiB: Reprint from [14].

## 2.8 Failure models

Referring to Section 2.7.1, it is evident that ISC occurs due to separator failure in case of indentation loading. According to [15], which aligns with the compression loading scenario pertinent to this case, the appropriate failure models to consider are Volumetric Strain and Maximum Shear Strain, based on the understanding from Section 2.7.1 Stage 5.

The Maximum Shear Strain model is particularly relevant because it directly relates to the mechanical deformation and failure mechanisms that occur under compressive forces. This model helps identify critical shear points where the separator is likely to fail, leading to ISC.

The Volumetric Strain model is essential for understanding the overall deformation behaviour of the battery cell components under compression. This model evaluates how the material volume changes under stress, which is crucial for predicting the onset of mechanical failure in the separator and other cell components.

By considering both Maximum Shear Strain and Volumetric Strain, a comprehensive understanding of the failure mechanisms under compression can be achieved, ensuring an accurate prediction of ISC in the battery cell.

### 2.8.1 Maximum Shear strain

Shear strain refers to the deformation experienced by a material when it is subjected to a force that causes the particles within a continuous body to slide past each other. In the context of this study, it is crucial to understand shear strain as it directly impacts the integrity of the separator under mechanical stress.

Maximum shear strain represents the highest level of shear deformation within an

element. It is quantified by the change in angle between segments that were originally perpendicular within the element. This measure is particularly important for analysing the behaviour of the jelly roll and separator within the battery cell, as these components are susceptible to shear forces during compression. Understanding the maximum shear strain helps in identifying potential points of failure, which can lead to internal short circuits (ISC) in the battery, and the maximum shear strain in LS-Dyna [16] is represented in eq. (2.82).

$$\epsilon = \left[\frac{1}{9}\left((\epsilon_x - \epsilon_y)^2 + (\epsilon_y - \epsilon_z)^2 + (\epsilon_z - \epsilon_x)^2\right) + \frac{1}{6}\left(\gamma_{xy}^2 + \gamma_{yz}^2 + \gamma_{zx}^2\right)\right]^{\frac{1}{2}} \tag{2.82}$$

### 2.8.2 Volumetric Strain

In a continuum body, three mutually perpendicular planes, known as principal planes, exist at any given point. The absence of shear stresses characterises these planes. Similarly, there are planes where only normal strains occur, and shear strains are absent. These planes are also called principal planes, and the strains experienced on them are termed Principal.
The principal strains are denoted as $\epsilon_1$, $\epsilon_2$, and $\epsilon_3$, while the normal strains are denoted as $\epsilon_{11}$, $\epsilon_{22}$, and $\epsilon_{33}$.
The strain invariants [17] in terms of principal strains are written as

$$\begin{aligned} J_1 &= \epsilon_1 + \epsilon_2 + \epsilon_3 \\ J_2 &= \epsilon_1\epsilon_2 + \epsilon_2\epsilon_3 + \epsilon_3\epsilon_1 \\ J_3 &= \epsilon_1\epsilon_2\epsilon_3 \end{aligned} \tag{2.83}$$

The physical interpretation of the invariants ($J_1$, $J_2$, and $J_3$) depends on the tensor they are computed from, whether it's a stress or strain tensor.

1. $J_1$ is directly related to the hydrostatic component of the tensor. In stress analysis, it represents the mean stress or the average pressure acting on a material in all directions. In strain analysis, it corresponds to the volumetric strain, indicating the overall change in the volume of the material.
2. $J_2$ is typically associated with the deviatoric aspects of stress and strain, although it may not exclusively represent them. In stress analysis, it characterises the shear stress or the tendency of the material to deform under shear forces. In strain analysis, it reflects the distortion or the non-uniform deformation within the material.
3. $J_3$ does not seem to hold a direct physical significance as a stress or strain tensor determinant. While $J_1$ and $J_2$ have clear physical interpretations, $J_3$ does not have a straightforward interpretation in stress or strain analysis. However, it's important to note that the determinants of stress and strain tensors should not be confused with the determinant of a deformation gradient, a separate concept used in continuum mechanics to describe deformation in materials undergoing displacement.

$$\epsilon_{vol} = \epsilon_1 + \epsilon_2 + \epsilon_3 \tag{2.84}$$

# 3
# Methods

## 3.1 Test setup

The experiment consisted of two distinct loading conditions: in-plane and out-of-plane. The orientation of the loading scenarios are illustrated in Figure 3.1. These loads were imposed on four batteries, with two tests conducted for each loading condition. The model underwent quasi-static loading, a semi-circular rigid object was positioned on one side. At the same time, the other end was fixed, and the impactor was gradually inserted into the cell until thermal runaway occurred in a cell with a state of charge (SOC) of 100%.

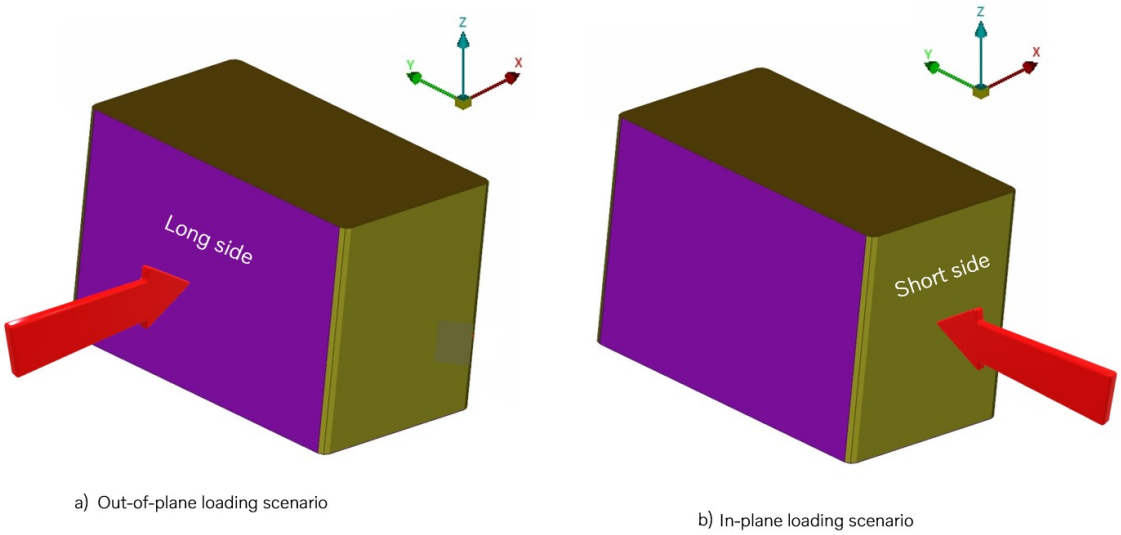


**Figure 3.1:** a) Out-of-plane loading and b) in-plane loading.

## 3.2 FE Model setup - LS Dyna

### 3.2.1 Jelly roll mesh sizing

The battery cell was segmented into mesh parts using solid and shell elements. The mesh sizing adhered to the standards set by Volvo Cars to meet the criteria necessary for a full-vehicle crash. To understand the behaviour of the jelly rolls, which represent the homogenised properties of the battery components, they were meshed

with hexahedron solid elements, each side ranging from 2.50mm to 3.34mm. These hexahedron elements were selected for their simplicity, which helped to reduce computational time. The casing and lid were meshed with 3 mm shell elements. Figure 3.2 displays the FE model of the battery cell and the jelly roll's mesh size.

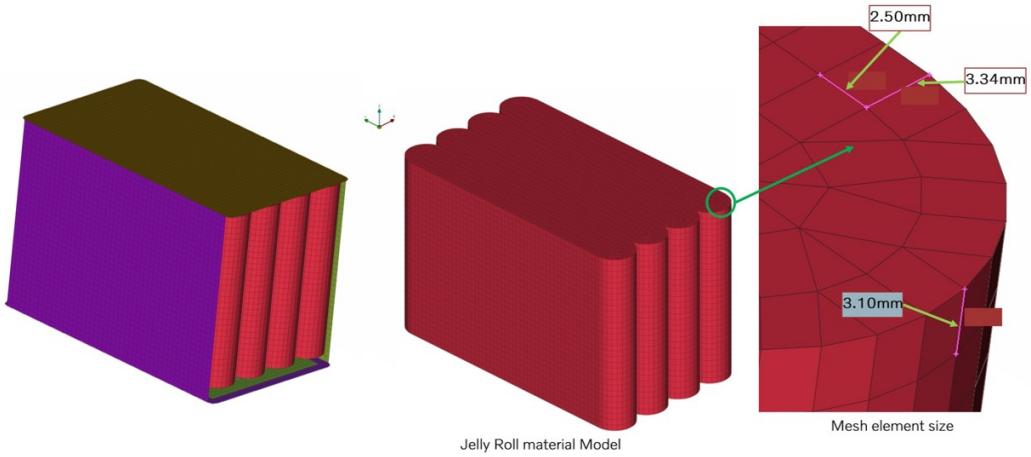


**Figure 3.2:** FE-model of battery cell.

### 3.2.2 Loads

The model is loaded at a rate of 1m/s for both both in-plane and out-of-plane loading scenarios as shown in Figure 3.3.

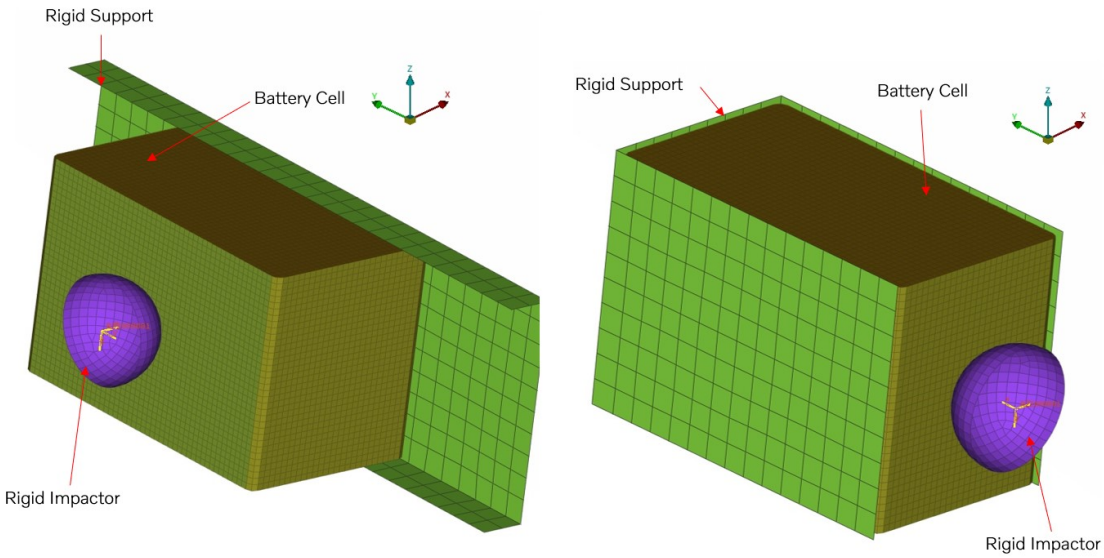


**Figure 3.3:** Two different load cases applied to the FE-model.

### 3.2.3 Boundary condition

As established in the test cases, out-of-plane and in-plane loading scenarios are examined here. Therefore, the model boundary conditions incorporate these two loading cases, defined as follows:

1. For case 1 illustrated in Figure 3.4 (a), i.e., out-of-plane loading, only one side (the rear part) of the battery is supported by a rigid support.
2. For case 2 illustrated in Figure 3.4 (b), i.e., in-plane loading, three sides of the battery are supported by a rigid support, with the load acting within the plane of action.

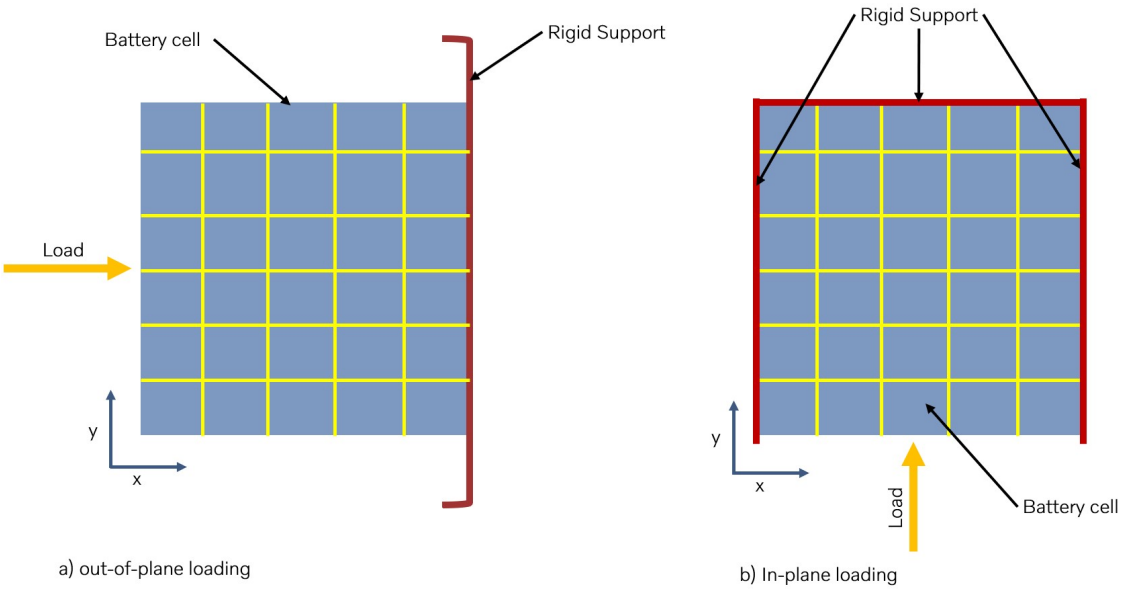


**Figure 3.4:** a) Out-of-plane loading scenario and b) In-plane loading scenario.

### 3.2.4 Battery cell material model

#### 3.2.4.1 Jelly roll material model

Research findings have revealed that battery materials exhibit anisotropic behaviour, leading to the adoption of the *MAT-MODIFIED-HONEYCOMB material model. This model enables the specification of nonlinear elastoplastic behaviour for normal and shear stresses, treating them as fully decoupled. Additionally, it incorporates a second yield surface to account for off-axis loading effects. However, the definition of this second yield surface poses a risk of shear mode collapse due to inadequate shear resistance. Finding a solution without altering the behaviour in uniaxial compression proved challenging. As a result, the model was enhanced with a third yield surface, allowing for the adjustment of shear and hydrostatic resistance independently of uniaxial behaviour [11].
The standard element formulation designated for this material is solid type 0, which corresponds to a nonlinear spring-type brick element. The recommended hourglass control by the manual is a type 2 viscous formulation specifically designed for one-point integrated solid elements [11].

After selecting the material model, it was crucial to establish the stress versus strain relationship for all directions (x, y, z) to determine the material hardening of the jelly roll model. For this purpose, the power law proposed by Wierzbicki, and Sahraei [18] was employed, incorporating the volumetric strain concept. This relation is expressed as follows:

$$\sigma_{vol} = A|\epsilon_{vol}|^n \tag{3.1}$$

Here, $A$ corresponds to the strength coefficient, $n$ represents the hardening exponent, and $\epsilon_{vol}$ represents volumetric strain. Initial parameter assumptions were made, resulting in values of 0.49, 0.45, and 0.15 for $A$, and exponents $n$ of 1.35, 1.0, and 1.8, respectively. However, these assumptions caused the material to behave too softly initially, due to the exponent values being above 1. Through an iterative simulation process to align the model's behaviour with real-life test data, the final values were adjusted to 0.6, 0.7, and 0.2 for strength coefficient ($A$), and 0.75, 0.9, and 1.05 for the hardening exponent ($n$), respectively. Figure 3.5 shows the load curves defined in the FE model for the x, y, and z directions.

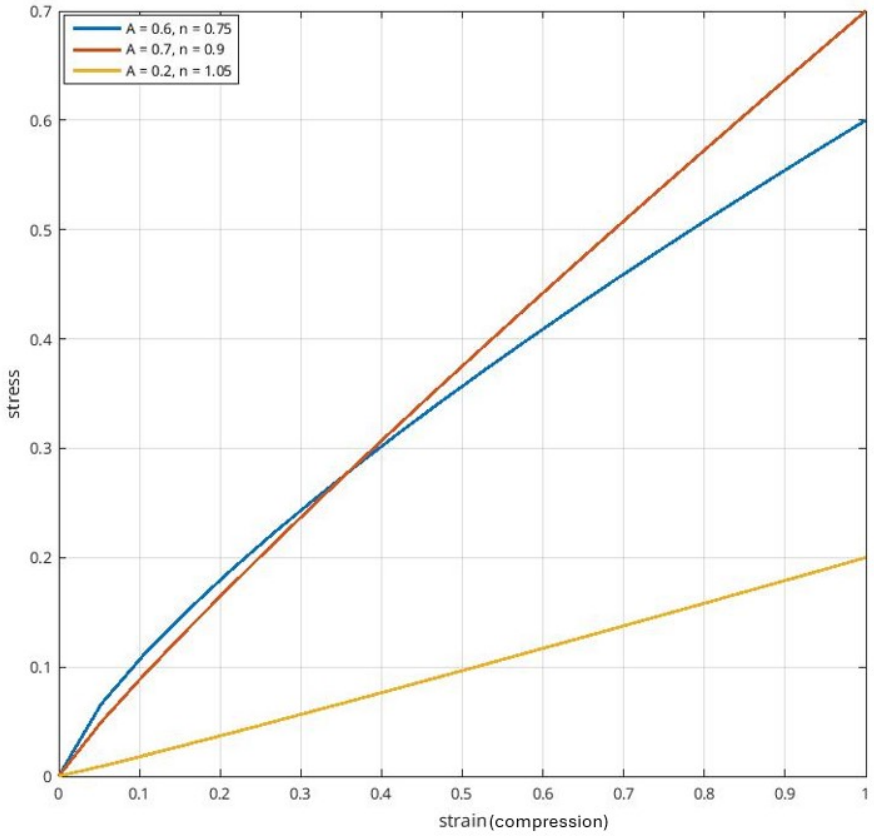


**Figure 3.5:** Load curve definition for hardening.

After developing the load input curves, the subsequent step involved scaling these curves to more accurately reflect realistic behaviour. This process utilised the scaling factor in the material card, which adjusts the load curve as needed. The scaling factor was applied to both the abscissa (x-axis) and ordinate (y-axis) axes, ensuring

that the curves were appropriately aligned to represent the material's response under the loading conditions. This adjustment was crucial for fine-tuning the model to achieve a more accurate simulation of the material behaviour.

The inputs for the material cards were,

- E - Young's modulus for compacted honeycomb material
- RO - Mass Density
- SIGY - Yield stress for fully compacted honeycomb
- LCA - Yield stress as a function of the angle off the material axis in degrees
- LCB - Load curve ID in the strong-axis
- LCC - Load curve ID in the weak-axis
- EAAU - Elastic Modulus in strong-axis uncompressed configuration
- EBBU - Elastic Modulus in the weak-axis uncompressed configuration
- ECCU - The initial yield stress in a simple shear uncompressed configuration
- GABU - Shear Modulus in the strong-weak-axis uncompressed configuration
- GBCU - Shear Modulus in the weak-weak-axis uncompressed configuration
- GCAU - Initial stress limit (yield) in hydrostatic compression
- AOPT - Material axes in this case are defined as locally orthotopic as defined in the subsection 3.2.4.2.
- SFA - Scale factor added to all the load curves for abscissa.
- SFO - Scale factor added to all the load curves for ordinate.

Scale factors, specifically SFA and SFO, are used to adjust the input load curves provided in Section 3.2.4.1. These factors serve to either increase or decrease the load curves in x and y-direction respectively, as the initial curves are not precise. LS-Dyna helps in refining the material response accordingly.

#### 3.2.4.2 Coordinate system

It is important to define a local coordinate system with 3 node numbers as recommended by LS DYNA manual [11]. Due to the anisotropic behaviour of the jelly roll, defining an accurate coordinate system within the material is essential, as it undergoes complex deformation. To address this, a locally orthotropic system, determined by element nodes, is employed, using the keyword AOPT = 0. In this system, the coordinate axes $a, b, c$ correspond to the global axes $x, y, z$, respectively. Following the guidelines by the manual, the primary direction is defined as the x-axis, while the z-axis is defined as the cross product of $x$ and $y$, i.e., $z = x \mathbf{x} y$, and the $y$-axis is computed as a cross product of $z$ and $x$ i.e., $y = z \mathbf{x} x$. Figure 3.6 illustrates the definition of an element coordinate system.

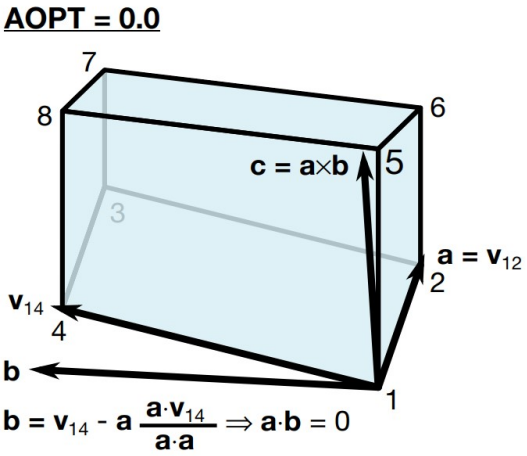


**Figure 3.6:** Material coordinate system for jelly roll solid elements [11].

#### 3.2.4.3 Battery cell casing material model

The external can of the battery cell is a deep-drawn, seamless aluminium material which ensures that the prismatic battery is leak-resistant and can withstand external shocks. Thus to account for these properties, material card *MAT-PIECEWISE-LINEAR-PLASTICITY is used to define the properties, the properties are defined in Table 3.1

**Table 3.1:** Material properties for battery cell casing.

| Property | Value |
|---|---|
| Density | $2.7 \times 10^{-6}$ kg/mm$^3$ |
| Young's Modulus | 70 GPa |
| Poisson's Ratio | 0.33 |
| Yield Strength | 140 MPa |

#### 3.2.4.4 Rigid support and impactor

The test support and impactor are made of steel. To simplify the CAE model of the test setup, the rigid body supporting the battery cell and the impactor intruding into the battery cell are both defined using the *MAT-RIGID material card.

### 3.2.5 Contact

In this case of a quasi-static loading test on the battery, maintaining contact among all components is necessary. The model comprises four jelly rolls, each in contact with the others, with the dynamic and static coefficients of friction set at 0.15. The static and dynamic coefficient of friction is assumed to be dependent on the relative velocity $\nu_{rel}$ of the surfaces in contact according to equation 2.28. To minimise numerical noise, common in crash simulation as in this case, the static and dynamic friction coefficients are made equal. The decay coefficient ($DC$) facilitates

the smooth transition of the net friction coefficient from static to dynamic. While a decay coefficient typically facilitates a smooth transition from static to dynamic friction, it is disregarded here and set to 0 since the focus is not on that transition. Global contacts *AUTOMATIC-SURFACE-TO-SURFACE were established, focusing on surface-to-surface interactions among the jelly rolls and between the jelly rolls and the cell casing. This also included interactions with the rigid support, battery, and impactor. The penalty method was employed to ensure consistent contact across all components.

## 3.3 Material model calibration

Following the establishment of the material model incorporating the defined load curves, the subsequent task involved correlating the force-displacement response curve in the FE model with the curve extracted from the test data. Due to time constraints, an optimisation tool LS-OPT was employed to achieve optimal behaviour for both in-plane and out-of-plane loading conditions.

### 3.3.1 LS OPT

According to the user manual [19], optimisation is defined as a process aimed at "achieving the best possible outcome for a given operation while adhering to specific constraints." In LS-OPT, a metamodel-based optimisation approach [19] is utilised to develop and optimise an approximate design model instead of directly simulating the design. This metamodel acts as a straightforward and cost-effective surrogate for the actual design. Once the metamodel is constructed, it can be employed to determine the optimal solution or, for multiple objectives, to identify the Pareto Optimal Front. The fundamental steps in this process are as follows:

1. **Point selection**: Identifying a set of points within the design space where simulations will be conducted to collect data.
2. **Run the simulations**: Execute simulations at the chosen points to gather the corresponding response data.
3. **Build the metamodels**: Construct mathematical models, such as regression models or neural networks, that approximate the system's behaviour based on the simulation outcomes.
4. **Execute the metamodel optimisations**: Use the metamodels to carry out optimisation algorithms, such as gradient-based methods or evolutionary algorithms, to determine the optimal solution or the Pareto optimal front.

### 3.3.2 Meta model-based optimisation

Here, 2 different strategies were considered to build a meta-model for optimisation.

#### 3.3.2.1 Sequential Strategy

Here, sequential sampling was utilised, selecting a default of 35 points for each iteration and setting a maximum of 20 iterations as the termination criteria. This

strategy provided the flexibility to stop the iterative process once the metamodels or optimal points achieved a satisfactory level of accuracy.

#### 3.3.2.2 Sequential Strategy with domain reduction

In this method, while the overall approach remains sequential, an adaptive domain reduction strategy is employed to speed up convergence. This strategy entails shrinking the subregion within the design space during each iteration, focusing on new sampling points within this reduced area. This adaptation aims to establish stopping tolerances, thereby improving convergence.

### 3.3.3 Material Model optimisation

The Sequential strategy with domain reduction method was used to optimise the material model, focusing on refining the load curve detailed in Section 3.2.4.

#### 3.3.3.1 Parametric modelling

**Table 3.2:** Material input parameters (normalised).

| Property | Value |
|---|---|
| Elastic Modulus (compressed) | 1 |
| Poisson's Ratio | 0.215 |
| Yield Strength | 0.203 |
| Elastic Modulus (uncompressed) in X direction | 0.851 |
| Elastic Modulus (uncompressed) in Y direction | 0.930 |
| Elastic Modulus (uncompressed) in Z direction | 0.874 |
| Shear Modulus (uncompressed) in XY direction | 0.358 |
| Shear Modulus (uncompressed) in YZ direction | 0.392 |
| Shear Modulus (uncompressed) in ZX direction | 0.365 |
| SFA in x direction | 0.0665 |
| SFA in y direction | 0.266 |
| SFA in z direction | 0.541 |
| SFO in x direction | 0.7313 |
| SFO in y direction | 0.294 |
| SFO in z direction | 0.481 |
| SFA in xy direction | 0.01 |
| SFA in yz direction | 0.01 |
| SFA in zx direction | 0.01 |
| SFO in xy direction | 0.01 |
| SFO in yz direction | 0.01 |
| SFO in zx direction | 0.01 |

The moduli values have been normalised to the highest value with respect to the elastic modulus (compressed). After selecting the meta-model building strategy, the subsequent stage entailed selecting the parameters influencing the material model's

behaviour. These parameters included elastic moduli, shear moduli, and scale factors impacting the load curves. A parametric investigation was conducted to grasp the influence of these parameters on the material response curve, followed by a sensitivity analysis to evaluate the effects of each parameter on the behaviour.
As the initial step for parameterisation, the material card selected for the jelly roll, specifically the *MAT-MODIFIED-HONEYCOMB material model, had all its input properties parameterised during the first iteration. The reason for this approach was to identify the variables that significantly impact material behaviour. For the initial guess, all parameters were set to continuous sampling. According to [19], continuous sampling is recommended because it typically results in a better distribution of points within the design space, leading to improved meta-model quality. The initial guess for the parameters is listen in Table 3.2.

## 3.4 Post-processing

The final results of the thesis were obtained using the META post-processor, where the strains were calculated. However, since META does not estimate volumetric strains directly, user-defined functions were developed to calculate these strains. The calculation of volumetric strains is based on strain invariant, as detailed in subsection 2.8.2.

# 4

# Results and Discussion

## 4.1 Test response

After conducting 4 tests, the force-displacement response was captured. The curves depicted in Figure 4.1 illustrate the force experienced by the test battery under quasi-static loading. Curves with higher peaks indicate out-of-plane (long-side) loading, and the change in direction at the peak suggests an occurrence of ISC in the battery cell, rendering it unable to bear further load. On the other hand, curves with lower load-bearing capacity and higher displacements represent in-plane (short-side) loading. It is important to note that in the case of the short-side loading scenario, the initial dip observed in the curve can be attributed to displacement occurring in the rigid body support, along with the battery cell, caused by unintended fixture motion in the test.

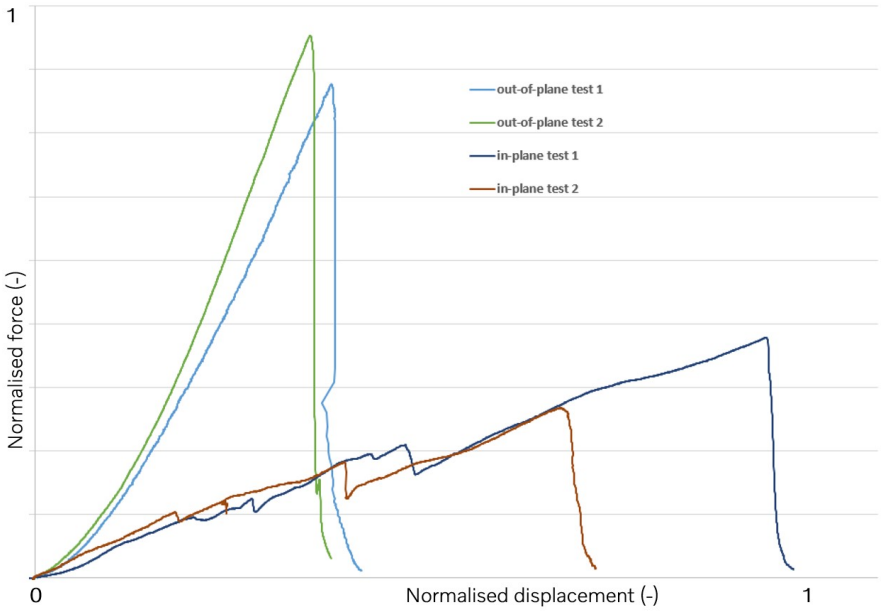


**Figure 4.1:** Force v/s Displacement response from test data.

## 4.2 In-plane loading material model response

This section analyses the material behaviour response under in-plane loading by correlating it with test data 1 and 2. According to the guidelines provided in the LS-DYNA Manual [11], the element formulation (ELFORM) was set to 0, and the hourglass control type was set to 2. The input load curves depicted in Figure 3.5 were plugged into the material card. This study aimed to understand the behaviour and parameters influencing the material response under in-plane loading conditions compared to test cases 1 and 2.

During the initial phase, the material model for the jelly roll was optimised to align with the results of test cases 1 and 2. This optimisation was essential to comprehensively understand the various parameters set during the optimisation process that affect the material behaviour. By refining these parameters, the goal was to achieve a more accurate representation of the material's response under the specified loading conditions. This iterative approach allowed for a detailed analysis of the factors impacting the material's performance, ensuring that the model closely matched the experimental observations. The final parameters that were derived from the optimisation for test cases 1 and 2 are shown in the Table 4.1

**Table 4.1:** Material parameters (normalised) for in-plane load; correlated against test cases 1 & 2.

| Variables | Correlation v/s test 1 | Correlation v/s test 2 |
|---|---|---|
| Elastic Modulus (compressed) | 0.820 | 0.788 |
| Poisson's Ratio | 0.34 | 0.34 |
| Yield Strength | 150 | 150 |
| EAAU | 0.994 | 1 |
| EBBU | 0.934 | 0.917 |
| ECCU | 1 | 0.979 |
| GABU | 0.415 | 0.417 |
| GBCU | 0.389 | 0.382 |
| GCAU | 0.416 | 0.414 |
| SFA in x direction | 0.499 | 0.491 |
| SFA in y direction | 0.432 | 0.448 |
| SFA in z direction | 0.282 | 0.269 |
| SFO in x direction | 0.102 | 0.102 |
| SFO in y direction | 0.0132 | 0.0105 |
| SFO in z direction | 0.396 | 0.392 |
| SFA in xy direction | 0.311 | 0.375 |
| SFA in yz direction | 0.486 | 0.468 |
| SFA in zx direction | 0.312 | 0.310 |
| SFO in xy direction | 0.238 | 0.242 |
| SFO in yz direction | 0.177 | 0.177 |
| SFO in zx direction | 0.329 | 0.322 |

The moduli values have been normalised to the highest value with respect to the elastic modulus for each case.
The elastic modulus varies between test 1 and test 2, as illustrated in Table 4.1. This variation is evident when examining the material response curves in Figure 4.2. The correlated elastic moduli for test 1 are in general slightly higher than those for test 2, which aligns with the physical interpretation of the material's behaviour. The slope of the correlation curve for test 1 is steeper than that for test 2, indicating a higher stiffness in the material under the conditions of test 1. This pattern is also observed for other variables, reflecting differences in the material's response to different loading scenarios. These variations highlight the importance of parameter optimisation to capture the material's behaviour under various testing conditions accurately.

Comparing this with Table 3.2, it is evident that the initial material parameters and guesses were not accurate. This optimisation process provided a better understanding of the parameters affecting the material's behaviour.

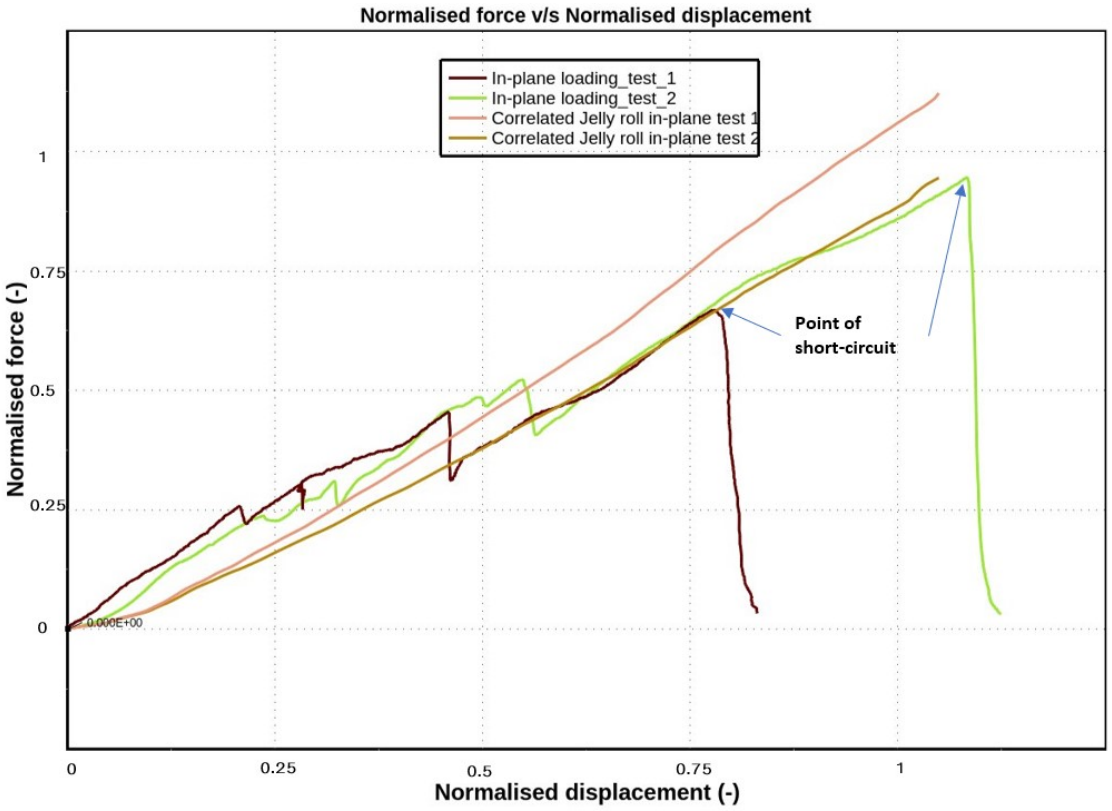


**Figure 4.2:** Force - Displacement response in-plane both cases.

### 4.2.1 LS DYNA Simulation

An LS-DYNA simulation was performed using the parameters obtained from Table 4.1. Figure 4.3 shows the maximum shear strain simulation results.

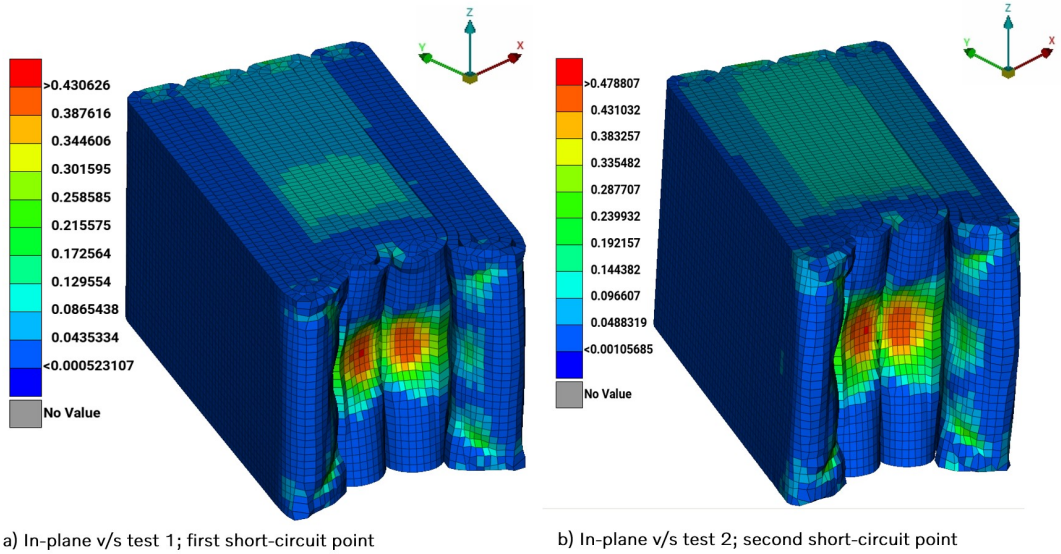


**Figure 4.3:** Maximum shear strain at ISC intrusion level for in-plane loading, test 1 v/s test 2.

This simulation revealed some intriguing material behaviour, particularly concerning the elements' response. It was observed that the elements were (initially) experiencing hourglassing, a phenomenon where elements exhibit unrealistic zero-energy deformation modes. This non-physical distortion results in inaccurate stress and strain predictions, leading to unreliable simulation results. The occurrence of hourglassing indicates that the selected hourglass control type for the chosen element formulations might not be appropriate to capture the actual behaviour of the material under the given loading conditions. Consequently, further optimisation and adjustment of the hourglass control type are necessary to mitigate hourglassing and ensure a more accurate representation of the material behaviour in the simulation. Testing the hourglass control on the developed material model revealed significant distortion and undesired material deformation in all directions. Referring to [20] and the LS-DYNA manual [11], it became clear that hourglass control type 6 is the most suitable for this case as compared to the one recommended by LS-DYNA manual explained in the subsection 3.2.4. The guidelines recommend hourglass control type 6 for scenarios where:

- Elements have large aspect ratios (greater than 2)
- Elements start or become significantly skewed
- The material is very soft (such as foam, honeycomb, or rubber)

Implementing hourglass control type 6 mitigated these issues and provided a more accurate simulation of the material behaviour under the given conditions.

## 4.3 Out-of-plane loading material response

After implementing the hourglass control type and reiterating for in-plane loading, the next step was to implement the same parameters and see the material behaviour by using the variables from 4.1 as the initial input for the out-of-plane load case, In this section, the material behaviour response to out-of-plane loading is analysed by correlating it with test data from tests 1 and 2 through an optimisation process for out-of-plane loading. The material model is correlated with test cases 1 and 2 for out-of-plane loading and the parameters are listed in the Table 4.2. The optimisation study for the out-of-plane loading revealed that the elastic modulus varies between test 1 and test 2, as illustrated in Table 4.2. This variation is evident when examining the material response curves in Figure 4.4. The slope of the correlation curve for test 1 is steeper than that for test 2, indicating a higher stiffness in the material under the conditions of test 1.

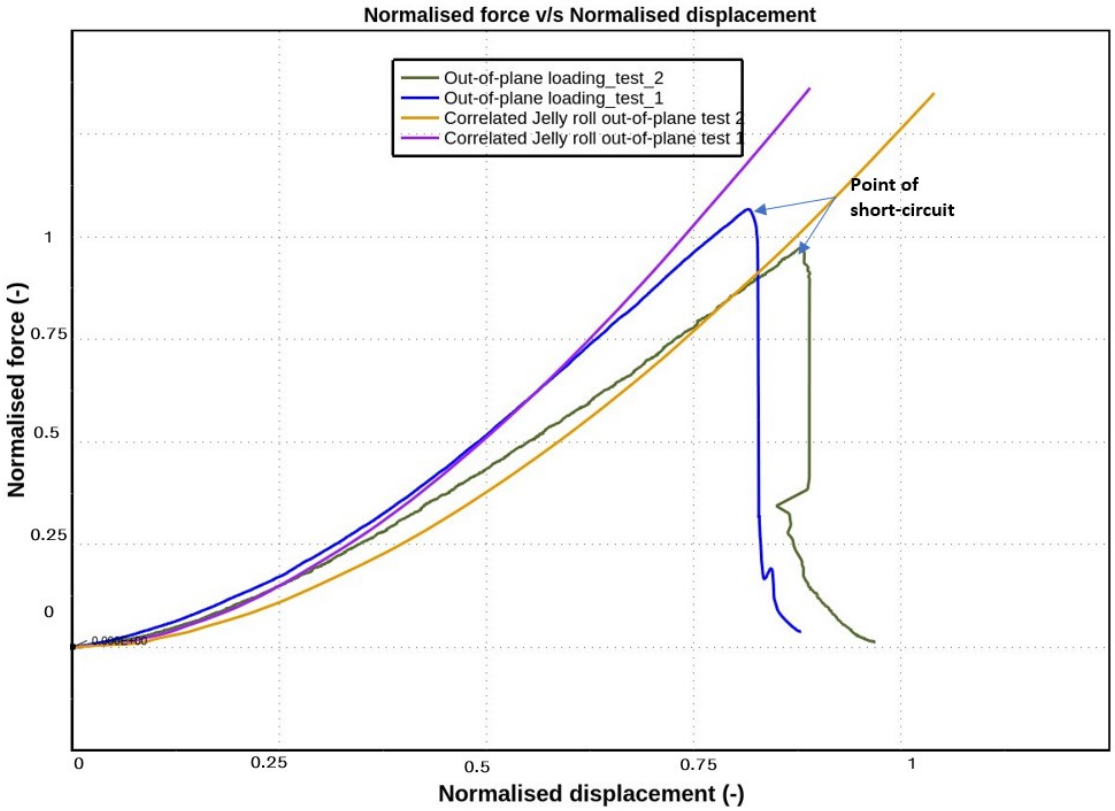


**Figure 4.4:** Force - Displacement response out-of-plane both cases.

**Table 4.2:** Material parameters (normalised) for out-of-plane load; correlated against case 1 & 2.

| Variables | Correlation v/s test 1 | Correlation v/s test 2 |
|---|---|---|
| Elastic Modulus (compressed) | 0.872 | 0.828 |
| Poisson's Ratio | 0.34 | 0.34 |
| Yield Strength | 150 | 150 |
| EAAU | 0.861 | 1 |
| EBBU | 0.947 | 0.339 |
| ECCU | 1 | 0.46 |
| GABU | 0.32 | 0.421 |
| GBCU | 0.338 | 0.386 |
| GCAU | 0.374 | 0.417 |
| SFA in x direction | 0.272 | 0.217 |
| SFA in y direction | 0.1 | 0.152 |
| SFA in z direction | 0.5 | 0.499 |
| SFO in x direction | 0.05 | 0.071 |
| SFO in y direction | 0.3827 | 0.3721 |
| SFO in z direction | 0.1 | 0.01 |
| SFA in xy direction | 0.183 | 0.094 |
| SFA in yz direction | 0.276 | 0.493 |
| SFA in zx direction | 0.337 | 0.573 |
| SFO in xy direction | 0.150 | 0.174 |
| SFO in yz direction | 0.2 | 0.48 |
| SFO in zx direction | 0.337 | 0.144 |

The moduli values have been normalised to the highest value with respect to the elastic modulus for each case.

### 4.3.1 LS DYNA Simulation

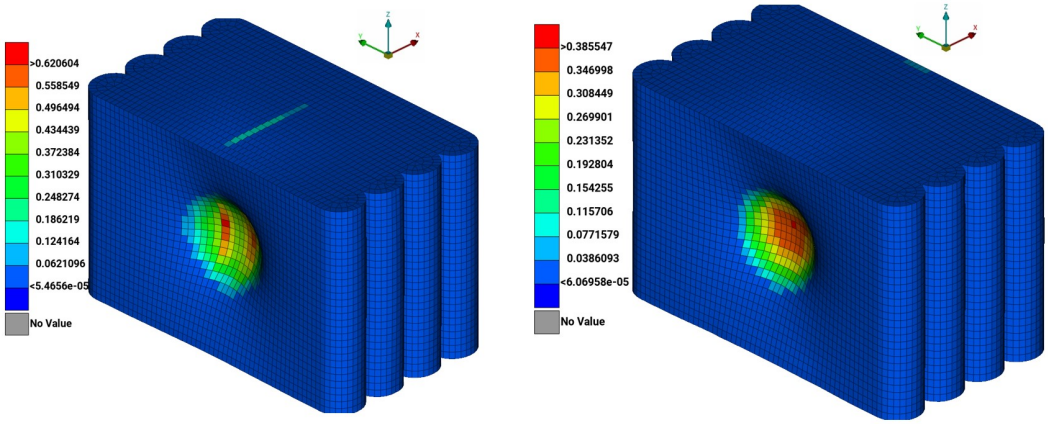


a) Out-of-plane v/s test 1; first short-circuit point

b) Out-of-plane v/s test 2; second short-circuit point

**Figure 4.5:** Maximum shear strain at ISC intrusion level for out-of-plane loading, test 1 v/s test 2.

An LS-DYNA simulation was performed using the parameters obtained from Table 4.2. Figure 4.5 shows the simulation results for maximum shear strain.

The plotted figure in 4.5 illustrates that the material exhibits a relatively stiff response at the loading point and becomes softer in the y-direction. However, in the correlation with test case 2, the material appears somewhat softer in the plane of loading, while maintaining its stiffness in the y-direction.

## 4.4 In-plane and Out-of-plane combined material response

Following the development of various material models tailored to different loading scenarios, the subsequent phase aimed to create a fully homogenised material model suitable for out-of-plane and in-plane loading conditions using identical parameters. The LS opt parameterisation study proved instrumental in identifying the key variables with significant impacts and determining the ranges within which these variables operate. This approach reduced computational time and enhanced efficiency by optimising the material model parameters.
The variables obtained after the final combined optimisation are shown in Table 4.3.

**Table 4.3:** Material parameters (normalised) for combined in-plane and out-of-plane load; correlated against all the test cases.

| Variables | Correlation in-plane and out-of-plane |
|---|---|
| Elastic Modulus (compressed) | 0.667 |
| Poisson's Ratio | 0.34 |
| Yield Strength | 150 |
| EAAU | 1 |
| EBBU | 0.68 |
| ECCU | 0.6 |
| GABU | 0.373 |
| GBCU | 0.126 |
| GCAU | 0.24 |
| SFA in x direction | 0.241 |
| SFA in y direction | 0.305 |
| SFA in z direction | 0.440 |
| SFO in x direction | 0.051 |
| SFO in y direction | 0.0105 |
| SFO in z direction | 0.250 |
| SFA in xy direction | 0.08 |
| SFA in yz direction | 0.427 |
| SFA in zx direction | 0.450 |
| SFO in xy direction | 0.14 |
| SFO in yz direction | 0.182 |
| SFO in zx direction | 0.419 |

The moduli values have been normalised to the highest value.

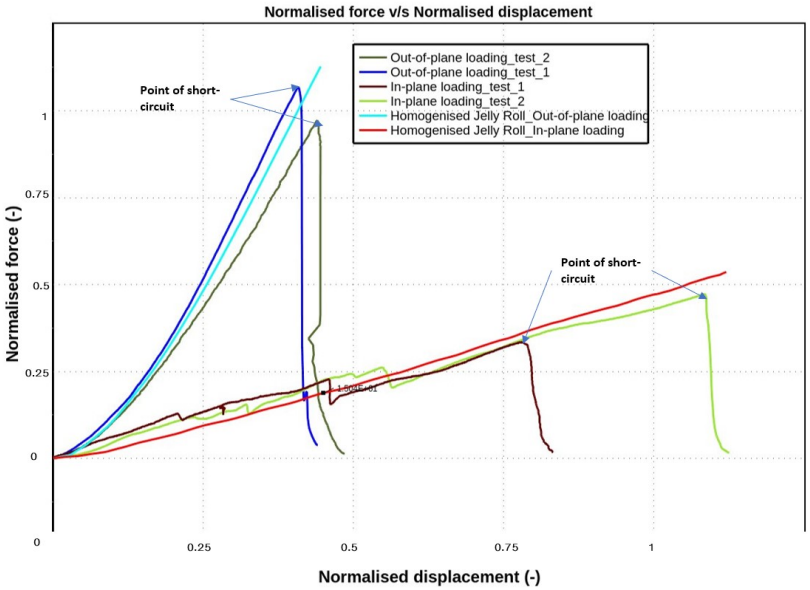


**Figure 4.6:** Force - Displacement response optimised material model, all load cases.

### 4.4.1 LS DYNA Simulation

The LS-DYNA simulation, utilizing the parameters derived from Table 4.3, provided insights into the material's response under different loading conditions. The simulation focused on analysing the maximum shear strain, a critical parameter for assessing material deformation and failure. Figures 4.7 and 4.8 present visual representations of the simulation results, offering valuable insights into the material's behaviour.

Upon assessing the fringe plots and Force v/s Displacement plots shown in Figure 4.6, it became apparent that the material exhibited significant stiffness when subjected to out-of-plane loading (x-axis). This stiffness could be attributed to the material's inherent properties and response to external forces acting in that direction. However, the material's behaviour under in-plane loading (y-axis ) presented a more complex scenario. While the overall response appeared satisfactory when viewed in the plot depicted in Figure 4.6, a closer inspection of Figure 4.7 revealed a softer response specifically in the in-plane direction (y-axis).

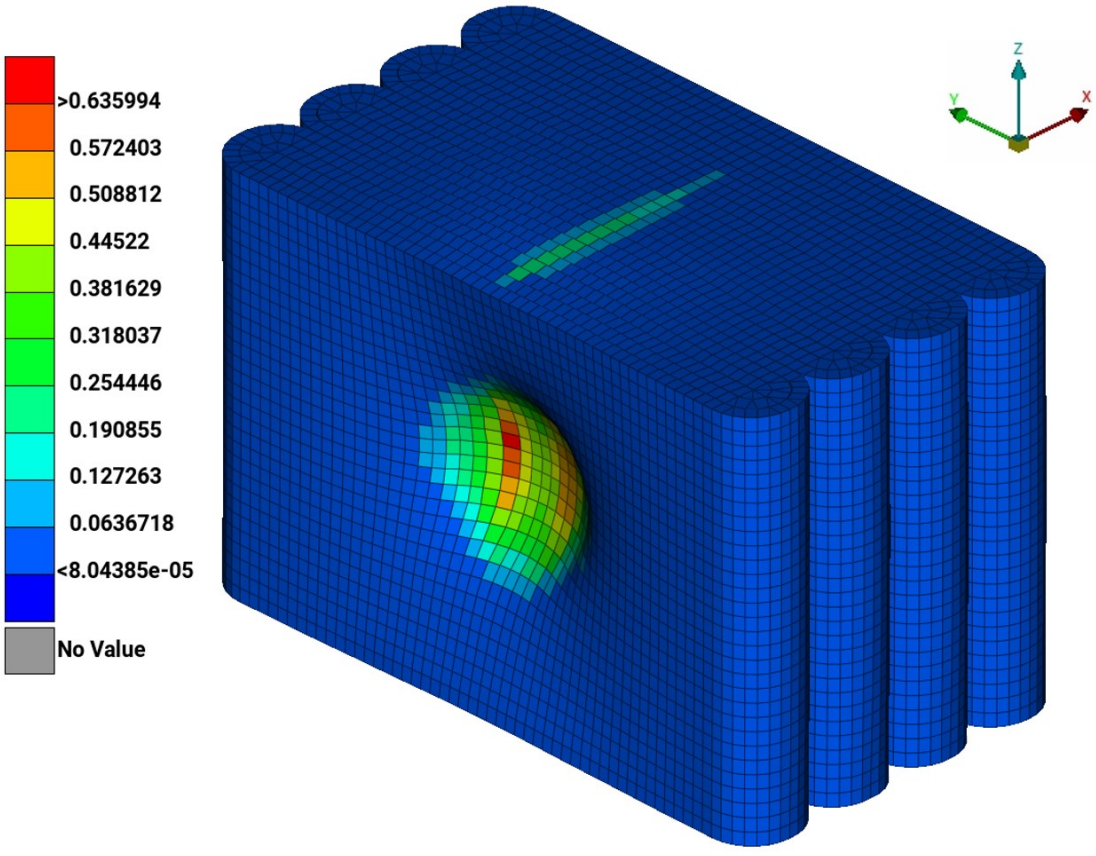


**Figure 4.7:** Maximum shear strain plot for the optimised material model at ISC intrusion level, out-of-plane loading.

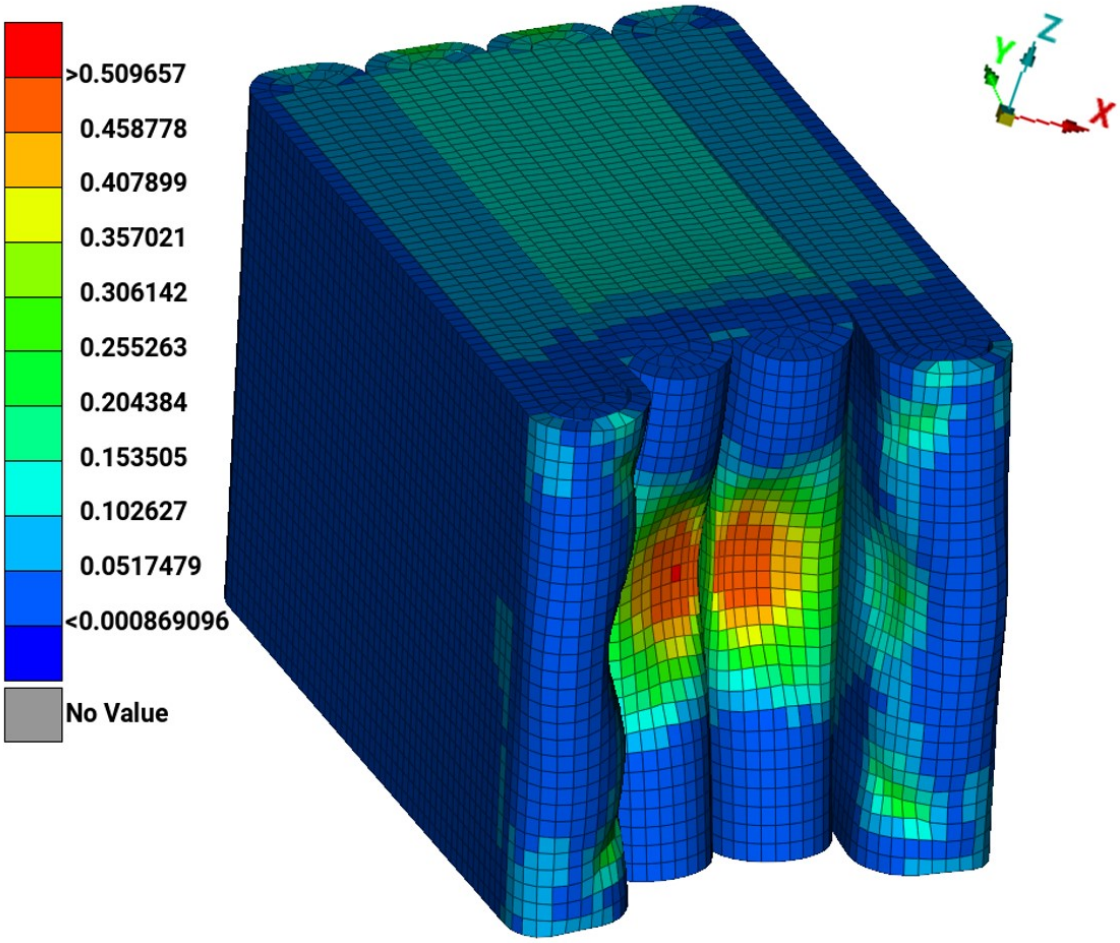


**Figure 4.8:** Maximum shear strain plot for the optimised material model at ISC intrusion level, in-plane loading.

## 4.5 Failure model implementation

After comprehending and refining the material response, the subsequent phase involved integrating the failure models into the post-processor to anticipate the short-circuit occurrence in the Li-ion battery. The objective of this section is to verify if the failure strain thresholds align with each other, given that the material model utilised is the same across all the load cases.

### 4.5.1 Maximum Shear strain

The maximum shear strains were determined for both in-plane and out-of-plane loading conditions from the impact model, and Figure 4.9 illustrates the material behaviour.

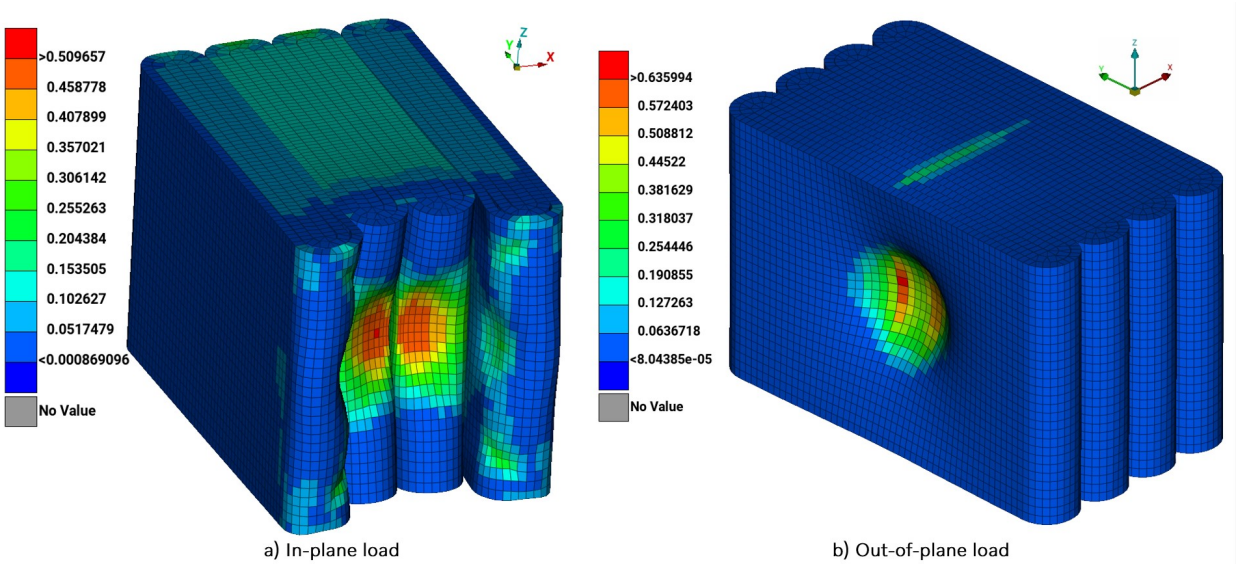


**Figure 4.9:** Maximum Shear strain comparison for a) In-plane loading b) Out-of-plane loading.

### 4.5.2 Volumetric strain

Volumetric strains were determined by establishing user-defined functions in the post-processor, facilitating the extraction of fringe plots from the impact model. The Figure 4.10 illustrates the material behaviour.

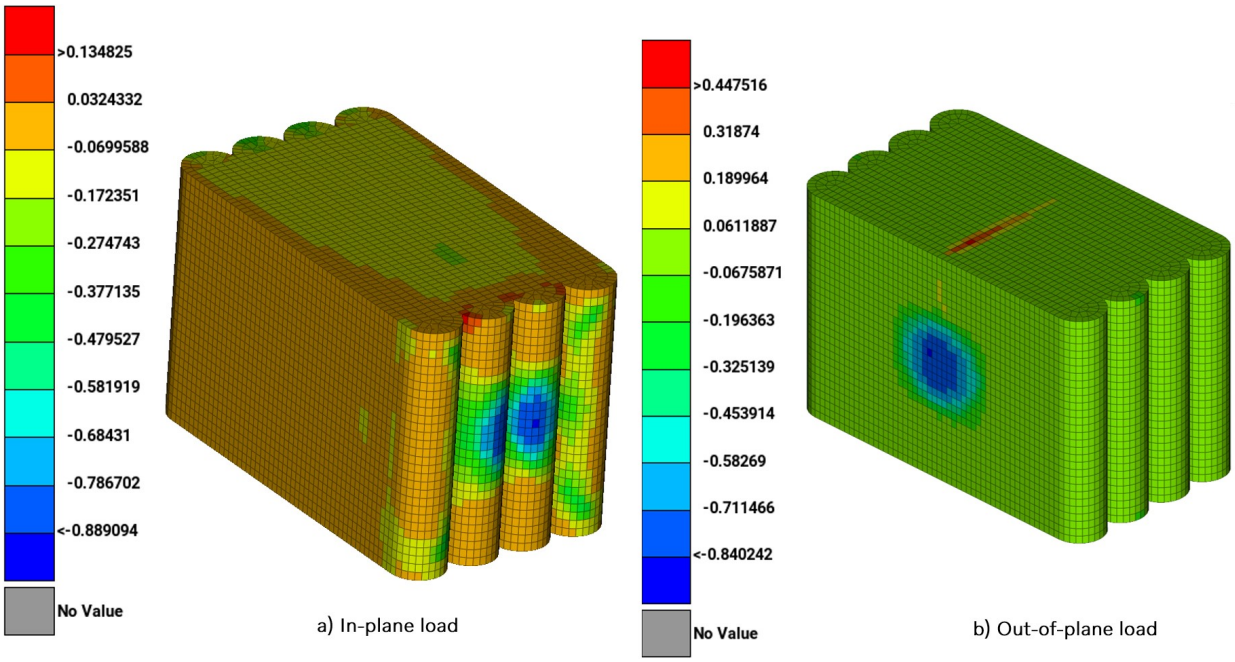


**Figure 4.10:** Volumetric strain comparison for a) In-plane loading b) Out-of-plane loading.

The analysis presented in subsection 4.5.1 and 4.5.2 delves into the discrepancy between the predicted values of maximum shear strain and volumetric strain for out-of-plane and in-plane loading conditions at the onset of short-circuit. The findings reveal contrasting trends between the two types of strain, shedding light on the material behavior under different loading scenarios.

In subsection 4.5.1, it is observed that the maximum shear strain exhibits a significant difference between out-of-plane and in-plane loading, with the latter showing a lower value. This discrepancy, amounting to approximately 30%, raises concerns regarding the reliability of the outcomes.

Conversely, in subsection 4.5.2, the analysis of volumetric strain portrays a more consistent behavior between out-of-plane and in-plane loading conditions. While there is a disparity of around 5% between the two scenarios, the difference is comparatively minor, suggesting a higher level of reliability in the simulation outcomes. This consistency lends credibility to the predictive capabilities of the material model under varying loading conditions.

# 5
# Conclusion

From the results discussed in the previous chapter, Table 4.3 indicates that the material exhibits anisotropic behaviour, confirming our earlier assumption in subsection 3.2.4 that the battery's material model is anisotropic, with distinct mechanical properties in various directions.

The guidelines recommended that for the *MAT-MODIFIED-HONEYCOMB material model, the hourglass control type should be 2 for the said element formulation, but the results from Section 4.2.1 suggest that for large deformation, and soft material (in this case), the hourglass control type 6 gives more stable result thus preventing hourglassing (element distortion). Thus, it is recommended to use the hourglass control type 6 for this material model under quasi-static loading.

While the material model appears to align with the test data curves, it is also important to observe the expansion of elements in the y (in-plane) direction at the simulation's centre, as illustrated in Figure 4.7. Interpreting the fringe plot indicates that the material lacks stiffness in the y (in-plane) direction, calling for further investigation.

However, it's crucial to acknowledge the limitations inherent in the modelling assumptions and the available test data. For example, the challenge of achieving a normal distribution of short-circuit points poses significant hurdles in accurately assessing the validity of the simulation results. Therefore, while the failure models exhibit promising performance, the inherent uncertainties emphasise the need for further refinement and validation to ensure the accuracy and reliability of the predictive capabilities.

# 6
# Future Scope

## 6.1 Material model input curves refinement

Section 3.2.4 presents the material model (under compression) input curves for hardening based on the power law, which shows the relationship between stress and strain. However, [21] introduces an alternative parameterisation that includes a constant term, $B$, in the equation $\sigma = A\epsilon^n + B$. Here, $B$ represents a constant parameter, $A$ denotes the strength coefficient value, and $n$ is the hardening exponent described in Section 3.2.4.
According to the formulation proposed by [21], the modification enhances predictive capability by effectively capturing the gradual increase of stress at small strains and the more rapid stress increase at larger strains. This refined approach accommodates a wider spectrum of material behaviours, thereby significantly improving the accuracy of stress-strain response predictions.

## 6.2 Study on Element formulation for the given model

In Section 4.2.1, it was noted that diverging from the recommended hourglass control type resulted in improved material simulation responses, particularly regarding in-plane behaviour. This observation prompts an investigation into how the material reacts to alternative hourglass control types within the same element formulation.
The decision to explore different hourglass control types stems from the finding that deviating from the recommended approach enhanced material behaviour. Therefore, examining how varying element formulations affect material behaviour and other optimisation parameters is crucial.
By delving into these aspects, we aim to deepen our comprehension of battery material responses and uncover potential avenues for refining simulation methodologies. This exploration has the potential to enhance the accuracy of predictions and optimise design processes.

## 6.3 Material mesh refinement

In Section 4.4.1, a notable issue of softness in the y-direction (in-plane) has been identified, necessitating a thorough investigation into its origins. The observed softness raises concerns regarding the reliability of the material's performance, especially

under specific loading conditions. One potential cause for this soft behaviour could be the coarse mesh resolution used in the jelly roll material model, highlighting the necessity for further refinement in meshing studies.
Understanding the root cause of this softness is crucial to ensuring the material's practical applicability. Comprehensive investigation and analysis are required to delve deeper into this issue and uncover any underlying factors influencing the material's response. By examining the mechanisms behind this soft behaviour, valuable insights can be gained to propose potential enhancements in material modelling and simulation methodologies.

## 6.4 Buckling consideration for refined layers in-plane loading

The current study addresses buckling within the specified number of layers. However, there is potential to enhance the finite element model by representing the jelly roll with more refined layers, which would allow for a detailed exploration of inter-layer buckling effects. This is crucial because buckling can induce out-of-plane deformations in the material, making it challenging to ascertain the occurrence of short-circuiting in the absence of parallel intrusions within the jelly roll.
Further investigation into buckling effects would provide a more comprehensive understanding of material behaviour and improve the accuracy of predicting short-circuit events. By integrating buckling considerations into the analysis, we can simulate real-world conditions more effectively and predict how the material will respond under various loading conditions.

## 6.5 Optimised Test Configuration and Increased Test Frequency

All tests encountered a significant challenge: instability in the test support system, leading to displacements in the battery support. This instability resulted in unreliable test outcomes, necessitating adjustments to the load-displacement response curve to address inconsistencies. To mitigate this issue, upgrading the test setup to ensure stable support is crucial for achieving more precise and dependable results.
Once the setup is optimised, the subsequent objective is to expand the dataset through additional tests. This expanded dataset will yield more data points related to short-circuit events, facilitating the establishment of a standard normal distribution (bell curve). Such a statistical model will enhance the accuracy of failure predictions by accommodating variability and providing a more nuanced understanding of potential failure modes.

## 6.6 Failure surface implementation

A robust approach to understanding and predicting short-circuit events in any material model involves the development of a dependable failure surface. This process entails gathering a significant number of test results and gaining a comprehensive understanding of the material's stress and strain behaviours. The failure surface encompasses yield stresses on each axis, enabling the creation of a failure envelope. By meticulously mapping out the stress and strain levels at which the battery cell fails under various loading conditions, a clear depiction of the material's failure characteristics emerges. This detailed understanding forms the foundation for constructing a failure surface that accurately represents how the material responds across different stress states. Armed with this information, we can more effectively predict occurrences of short-circuiting, as we have insight into the material's failure limits under diverse loading scenarios.
Therefore, investing in the development of a reliable failure surface for homogenised battery material models is crucial for enhancing the predictive capabilities of material models and ensuring the safety and reliability of engineering designs.
For further clarity, the schematic of the failure surface serves as a valuable visual aid, and Figure 6.1 illustrates an example of a failure surface for a 2-D model.

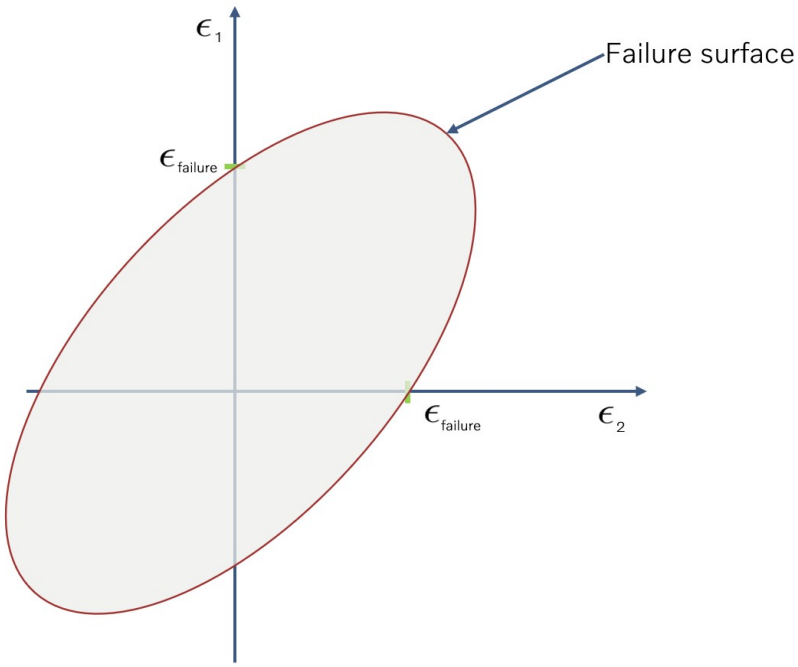


**Figure 6.1:** An example of a failure surface.

# Bibliography


[1] D. Lisbona and T. Snee, "A review of hazards associated with primary lithium and lithium-ion batteries," *Process Safety and Environmental Protection*, vol. 89, no. 6, pp. 434–442, 2011, Special Issue: Centenary of the Health and Safety Issue. DOI: https://doi.org/10.1016/j.psep.2011.06.022.

[2] J. Hong, Z. Wang, X. Zhang, W. Wang, Y. Chen, and T. Shan, "Collision-caused thermal runaway investigation of li-ion battery in real-world electric vehicles," *Applied Thermal Engineering*, vol. 236, p. 121 901, 2024. DOI: https://doi.org/10.1016/j.applthermaleng.2023.121901.

[3] C. Hendricks, N. Williard, S. Mathew, and M. Pecht, "A failure modes, mechanisms, and effects analysis (fmmea) of lithium-ion batteries," *Journal of Power Sources*, vol. 297, pp. 113–120, 2015. DOI: https://doi.org/10.1016/j.jpowsour.2015.07.100.

[4] A. Jana, D. R. Ely, and R. E. García, "Dendrite-separator interactions in lithium-based batteries," *Journal of Power Sources*, vol. 275, pp. 912–921, 2015. DOI: https://doi.org/10.1016/j.jpowsour.2014.11.056.

[5] G. Zhang, X. Wei, X. Tang, J. Zhu, S. Chen, and H. Dai, "Internal short circuit mechanisms, experimental approaches and detection methods of lithium-ion batteries for electric vehicles: A review," *Renewable and Sustainable Energy Reviews*, vol. 141, p. 110 790, 2021. DOI: https://doi.org/10.1016/j.rser.2021.110790.

[6] S. Shin, G. J. Jung, W.-J. Lee, C. Kang, and J. P. Wang, "Recovery of electrodic powder from spent lithium ion batteries (libs)," *Archives of Metallurgy and Materials*, vol. 60, pp. 1145–1149, Jun. 2015. DOI: 10.1515/amm-2015-0086.

[7] H. Heimes, A. Kampker, C. Offermanns, *et al.*, *Production of Lithium-Ion Battery Cell Components (2nd edition, 2023)*. Dec. 2023, ISBN: 978-3-947920-50-1.

[8] X. Huang, "Separator technologies for lithium-ion batteries," *Journal of Solid State Electrochemistry*, 2011. [Online]. Available: https://doi.org/10.1007/s10008-010-1264-9.

[9] P. Kelly, "An introduction to solid mechanics. solid mechanics part 1," *Solid Mechanics Lecture notes*, 2013. [Online]. Available: https://pkel015.connect.amazon.auckland.ac.nz/SolidMechanicsBooks/Part_I/index.html.

[10] M. Fagerström and M. Ekh, "Elasto-plasticity," *THE FINITE ELEMENT METHOD – STRUCTURES*, 2022.

[11] A. A. C. Livemore software Technology(LST), "Ls dyna keyword user's manual volume 1 and 2," *LS DYNA R12*, 2020.

[12] M. Ekh, R. Jänicke, F. Larsson, and K. Runesson, "Contact mechanics problems," *THE FINITE ELEMENT METHOD – SOLID MECHANICS*, 2022.

[13] A. A. C. Livemore software Technology(LST), "Ls dyna material model," *LS DYNA Theory Manual*, 2024.

[14] X. Zhu, H. Wang, X. Wang, *et al.*, "Internal short circuit and failure mechanisms of lithium-ion pouch cells under mechanical indentation abuse conditionsan experimental study," *Journal of Power Sources*, vol. 455, p. 227 939, 2020. DOI: https://doi.org/10.1016/j.jpowsour.2020.227939.

[15] C. Yuan, L. Wang, S. Yin, and J. Xu, "Generalized separator failure criteria for internal short circuit of lithium-ion battery," *Journal of Power Sources*, vol. 467, p. 228 360, 2020. DOI: https://doi.org/10.1016/j.jpowsour.2020.228360.

[16] B. C. S. I. AG, "Meta post processor version 23.1.x.," *META - post User Guide*, 2023.

[17] T.G.Sitharam and L.GovindaRaju, "Module 3: Analysis of strain," *Applied Elasticity for Engineers*, 2022.

[18] T. Wierzbicki and E. Sahraei, "Homogenized mechanical properties for the jellyroll of cylindrical lithium-ion cells," *Journal of Power Sources*, vol. 241, pp. 467–476, 2013. DOI: https://doi.org/10.1016/j.jpowsour.2013.04.135.

[19] A. A. C. Livemore software Technology(LST), "Ls opt keyword user's manual," *A Design Optimization and probabilistic analysis tool for the engineering analyst*, 2014.

[20] S. Shinde, Y. Song, and E. Sahraei, "Modeling electric vehicle's battery module using computational homogenization approach," *International Journal of Energy Research*, vol. 2023, pp. 1–19, Feb. 2023. DOI: 10.1155/2023/9210078.

[21] J. Xu, B. Liu, X. Wang, and D. Hu, "Computational model of 18650 lithium-ion battery with coupled strain rate and soc dependencies," *Applied Energy*, vol. 172, pp. 180–189, 2016. DOI: 10.1016/j.apenergy.2016.03.108.

**DEPARTMENT OF SOME SUBJECT OR TECHNOLOGY**
**CHALMERS UNIVERSITY OF TECHNOLOGY**
Gothenburg, Sweden
www.chalmers.se


CHALMERS
UNIVERSITY OF TECHNOLOGY